Coupled Halfwave Microstrip Resonators with Dumbbell Type Defected Ground Structure

Marin Nedelchev, Alexander Kolev[1]

Abstract – **The paper presents design, and simulation of coupled halfwave microstrip resonators with dumbbell type defected ground structures. For the design purposes, the coupling coefficient of the coupled resonators with different sizes of the dumbbell structure is investigated. Each topology is simulated in full-wave electromagnetic simulator and the coupling coefficient is extracted. Design graphs of the coupling coefficients are presented.**

Keywords – **microstrip coupled, resonator, coupling coefficient, defected ground, dumbbell**

I. INTRODUCTION

Microstrip filters are key components in the communication systems. They have continuous development in theory and realizations. Edge coupled halfwave microstrip filters are widely used in the practice because of their straighforward design process, easy manufacturing and adjustment, light weight and acceptable size on the printed circuit board. Therefore the improvement of the edge coupled filter characteristics and design process is worth.

One of the problems facing the wideband and ultrawideband filters is the realization of very small gaps between the coupled resonators and the fabrication tolerances connected to their manufacturing. The filter response is also affected by the precision of the manufacturing process of the small gaps. Utilizing different shaped slots in the ground plane of the microstrip line- defected ground structures (DGS) [1-5], it is possible to enhance the coupling coefficient and particularly the electrical coupling. There are proposed different types of DGS topologies in the literature not only for the analysis of the effect of the defects, but also for the implementation of the defects in various structures in microwave filters and devices. DGS is realized by introducing a shape defected on a ground plane so it will disturb the shielded current distribution depending on the shape and dimension of the defect. The disturbance at the shielded current distribution will influence the input impedance and the current flow of the design. The positions and lengths of the dumbbell sections control the response and insertion loss attenuation of the coupled lines. DGS increases the effective values of dielectric constant of substrates (ε_{reff}), thus, decreases the wavelength and the overall length of the design [6].

Fig.1 shows the different defected ground elements' shapes proposed in [1] and the most used DGS element is the dumbbell shaped.

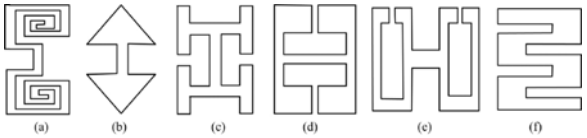

Fig.1 Types of DGS elements-(a) spiral head, (b) arrowhead-shot, (c) "H"-shape slot, (d) a square open-loop with a slot in middle section, (e) open-loop dumbbell and (f) interdigital DGS

Fig. 2 shows the edge coupled halfwave resonators with the dumbbell DGS in the ground plane.

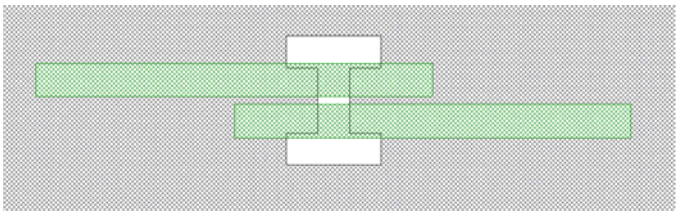

Fig.2 Parallel coupled halfwave resonators with dumbbell DGS

This paper researches the coupling coefficient between two edge coupled halfwave resonators with dumbbell DGS with respect to the variation of its dimensions. As the dumbbell DGS has a lot of degrees of freedom, the coupling coefficients for different dimensions of the dumbbell are computed using a full-wave electromagnetic simulator. The results of the research may be used in microstrip wideband filter design.

II. DUMBBELL DEFECTED GROUND STRUCTURE

All the simulations, design procedures in the paper are performed for dielectric substrate FR-4 with height 1.5mm, relative dielectric constant $\varepsilon_r = 4.4$ and loss tangent $tg\,\delta = 0.02$.

The form of the dumbbell type defected ground structure and its dimensions is shown on Fig. 3. It consists of an main slot connected on both ends to rectangular dumbbell heads.

[1]Marin Veselinov Nedelchev and Alexander Kolev –are with Dept. of Radiocommunication and Videotechnologies in Faculty of Telecommunication in TU –Sofia, N8, Kliment Ohridski bul., 1700 Sofia, Bulgaria. E-mail: mnedelchev@tu-sofia.bg

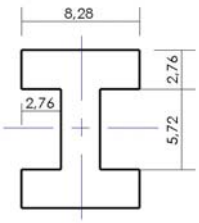

Fig.3. Form and size of the DGS (all sizes in mm)

The edge halfwave coupled resonators have width corresponding to the width of a line with a characteristics impedance of 50Ω. For the dielectric substrate FR-4, it is computed that the width of the line is $w = 2.76\,mm$.

Fig.4 shows two coupled resonators with length l=32.82mm for center frequency $f_0 = 2.4GHz$. The length is determined using a simulation in a full wave EM simulator.

Fig.4 Two coupled resonators with length 32.82mm and width 2.76mm

The responding coupling coefficient for synchronously tuned resonators can be calculated easily by the resonance frequencies of even and odd mode [2], when the coupled resonators are overcoupled:

$$k = \frac{f_e^2 - f_o^2}{f_e^2 + f_o^2} \tag{1}$$

A full wave EM simulator based on the Method of the Moments (MoM) is used to identify the resonance frequencies in the response [7,8].Figure 5 shows the frequency response of the coupled resonators, when there is no DGS and when we place a dumbbell DGS with the form and dimensions shown in Fig.3.

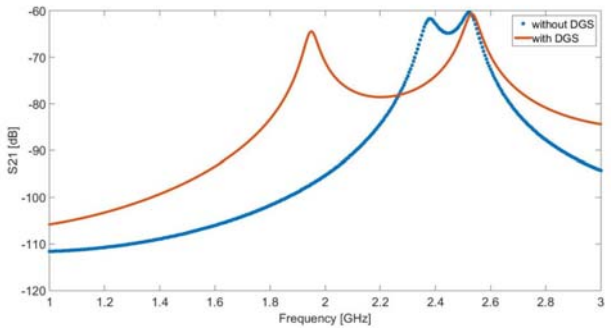

Fig. 5 Frequency response of the coupled resonators with and without dumbbell DGS

It is seen that the slot in the ground plane and the corresponding current disturbance enhances the electric coupling between the resonators. The split resonance frequency of the even mode, when DGS is used, is far away from the split resonance frequency, when no DGS is used. The odd mode resonance frequency is slightly higher than when no DGS is used. Consequently the dumbbell DGS under the coupled resonators enhances the electric part of the coupling coefficient. There is another physical description of this effect. In the microstrip coupled resonators without DGS, in the coupling mechanism many of the electric lines start from the top layer and end on the ground plane passing through the dielectric substrate. In the presence of the slot a part of these lines are forced to end on the other resonator, enhancing this way the electric part of the coupling. In this way the effective dielectric permittivity for even mode is much higher than the effective dielectric permittivity for odd mode. The DGS topology and size define the coupling coefficient behavior and enhancement.

This fact allows additional degrees of freedom in the synthesis of coupled resonator circuits [9].

III. PARAMETRIC ANALYSIS OF DGS SIZE IMPACT ON COUPLING COEFFICIENT

This section presents the results from the parametric study of the coupling coefficient between coupled halfwave resonators with dumbbell DGS in the ground plane. This parametric study will give the designer comprehensive understanding of the effect of the DGS under the coupled halfwave resonators. The study lead to design curves for coupled halfwave resonators with dumbbell DGS in the ground plane. It will assist the design process of microstrip filters synthesis in the ISM band of 2.4GHz.

The parametric study is performed in full wave EM simulator. Geometrically, the center point of the dumbbell DGS is placed in the center point of the coupled resonators.

Fig.6 shows the four parameter changes in the dumbbell DGS size- head height, head width, slot width and slot height.

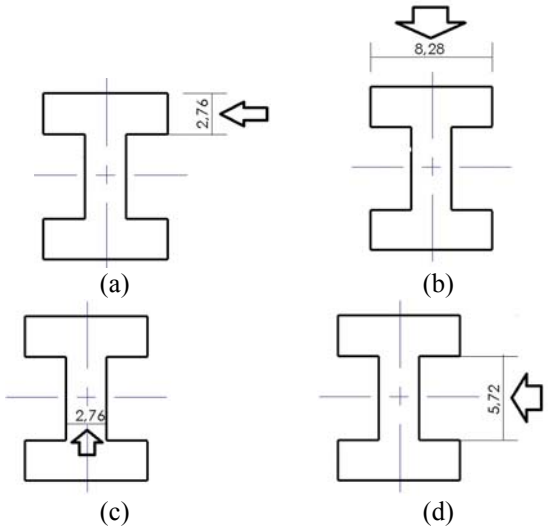

Fig.6 Dumbbell-type DGS size variation.
(a) height of the head, (b) width of the head, (c) width of the slot line (d) length of the slot line

Using full wave EM simulator, the split resonance frequencies in the magnitude response of the coupled resonators are obtained. Using Eq.1, the coupling coefficient is computed for heights of the dumbbell head from 0.2mm to 5mm. All the rest dimensions of the DGS topology remain unchanged. The corresponding family of curves for the

coupling coefficient are shown on Fig.7. Generally, the coupling coefficient is monotonically decreasing with the increasing the distance between the resonators. The gap between the coupled resonators is changed discretely from 0.2mm to 3.8mm. As the head of the dumbbell becomes bigger, the coupling coefficient is also increasing. For one and the same gap between the resonators, the value of the coupling coefficient can be at least two times bigger. The height of the dumbbell head has significant impact on the value of the coupling coefficient. It leads to technologically easy tuning of the coupling coefficient by changing the height during the filter adjustment.

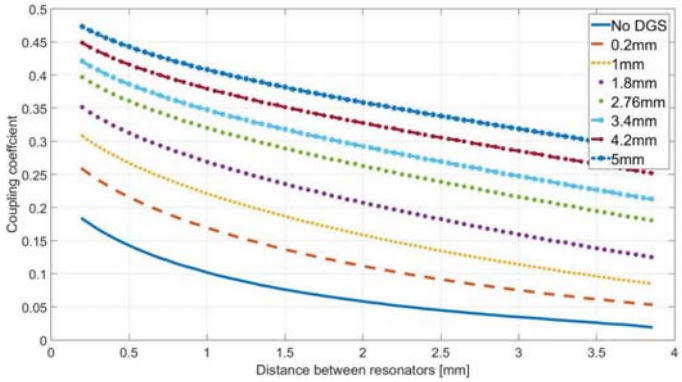

Fig.7 Coupling coefficient for height of the DGS head variation from 0.2mm to 5mm

Fig.8 shows the results from the study of the coupling coefficient, when the width of the DGS head is changed (as shown on Fig.6b). Again, the coupling coefficient is monotonic, but the big increase of the width does not lead to corresponding significant increase of the coupling coefficient. As it is seen from Fig.8, the presence of dumbbell DGS increase at least two times the value of the coupling coefficient.

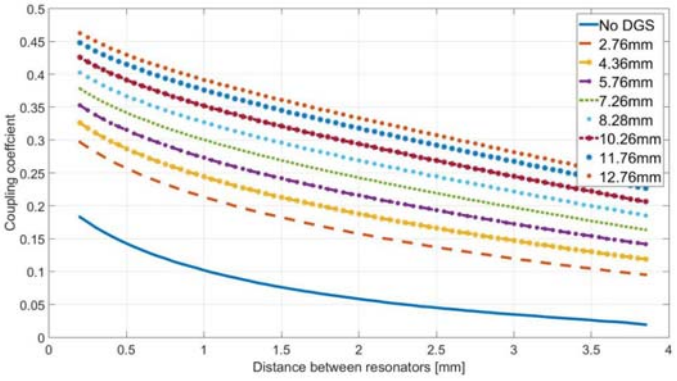

Fig.8 Coupling coefficient for width of the DGS head variation from 2.76mm to 12.76mm

Fig.9 figures out the results for the coupling coefficient when the slot of the dumbbell DGS is changed discretely from 0.2mm to 5.52. The current in the ground plane caused by the slot width is comparably small and the coupling coefficient enhancement is not so well pronounced like the cases when the other parameters are changed. The coupling coefficient increases in 30 to 50% compared to the smallest DGS slot width.

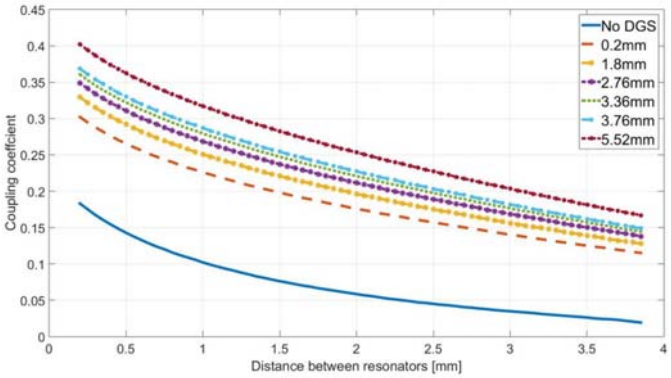

Fig.9 Coupling coefficient for width of the DGS slot variation from 0.2mm to 5.52mm

Fig.10 shows the coupling coefficient dependence on the distance between the resonators and the length of the slot of dumbbell DGS. The values of the coupling coefficient are at least 25% bigger than the values without DGS. The higher is the length, the bigger is the coupling coefficient.

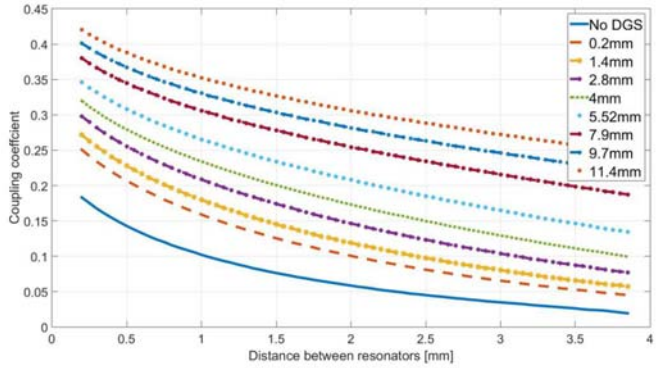

Fig.10 Coupling coefficient for length of the DGS slot variation from 0.2mm to 11.4mm

The parametric study of the coupling coefficient between coupled halfwave resonators confirm the assumption, that introduction of defects of specific topology in the ground plane of the microstrip technology will enhance it. This approach may be used in the wideband and ultrawideband microstrip filter design. From the study it was described the mechanism of the coupling coefficient increasing. The derived design graphs can be used by microstrip filter designers for the ISM band on 2.4GHz.

IV. Conclusion

This paper presents the coupling coefficient between two edge coupled halfwave resonators with dumbbell DGS with respect to the variation of its dimensions. The coupling coefficient between the resonators is derived using the split resonance method. The results from the studies are presented in several design graphs. They can be used in microstrip filter design in the ISM band on 2.4GHz on FR-4 substrate.

ACKNOWLEDGEMENT

The authors would like to thank Prof. Ilia Iliev, PhD, Dean of the Faculty of Telecommunication, Technical University of Sofia for the encouragement during the study and the bright ideas.

REFERENCES

[1] L.H. Weng, Y.C.Guo, X.W. Shi and X.Q.Chen, “An Overview on Defected Ground Structure”, Progress In Electromagnetics Research B., vol. 7, pp. 173-189, 2008.

[2] J.Hong, M.J Lancaster, "Microstrip Filters for RF/Microwave Applications", John Wiley and Sons Inc, 2001.

[3] G.Breed, “An Introduction to Defected Ground Structures in Microstrip Circuits”, High Frequency Electronics, pp 50-54, 2008.

[4] C.Carg, M.Kaur, “A Review of Defected Ground Structures (DGS) in Microwave Design”, International Journal of Innovative Research in Electrical, Electronics, Instrumentation and Control Engineering, Vol.2 Issue 3, 2004.

[5] S.K. Parui, S.Das, “A New Defected Ground Structure for Different Microstrip Circuit Applications ”, Radioengineering Vol. 16 No 1, 2007.

[6] D.M. Pozar, “Microwave Engineering”, John Wiley and Sons Inc., 2012.

[7] D.G. Swanson Jr, W.J.R Hoefer, “Microwave Circuit Modeling Using Electromagnetic Field Simulation”, Artech House 2003.

[8] D.B. Davidson, “Computational Electromagnetics for EF and Microwave Engineering”, Cambridge University Press, 2005.

[9] Z.Hou, X. Li and C. Hao, “Design of Wideband Filter Using Split-ring Resonator DGS”, Progress in Electromagnetics Research Symposi,China, March 24-28, 2008.

Effect of RF Receiver Nonlinearity on Mobile Telecommunication Systems

Youssef Abd Alrahman[1] and Ilia Iliev[2]

Abstract – **This paper proposes a modified model of signal-to-interference-and-noise ratio (SINR) which include the interference due to intermodulation products. Using this model, we study the effect of receiver's nonlinearity on the performance of telecommunication systems. We examine the problem of interference caused by intermodulation products generated by unwanted interference signals at receivers. Specifically, third-order intermodulation distortion (IMD3) that could be at frequencies within working band and drive circuits into saturation causing blocking for wanted signal at same frequency. Using Matlab software and nonlinear amplifier model, we achieve a practical calculations for third-order intercept point (IP3). Effect of Intermodulation products on SINR is shown using the third-order input intercept point (IIP3) specifications for GSM receiver and SINR modified model and Matlab software.**

Keywords – **SINR, GSM, RF receiver, Nonlinearity, Intermodulation.**

I. INTRODUCTION

In according to manage the increasing in the number of mobile subscribers around the world and their demands, more operators and base stations and frequencies reuse should be achieved. Which lead to a diverse range of challenges in frequency planning. Most important one is intermodulation because - as an example - third-order intermodulation products generated by two GSM-1800 signals could fall in UMTS band and interfere with one UMTS signal [1]. Thus, although mobile stations receive desired signals only from their operating base station, high-power signals from the neighboring base stations for another service providers, regardless of their carrier frequencies, may cause desensitization and blocking by forcing their circuits into saturation.

The intermodulation in mobile nonlinear systems can generate two different types of interference: the one that is called in-band, that is generated inside the GSM-900, GSM-1800 or UMTS band and is derived from inside frequencies, and the out of band interference that is generated mixing terms from the GSM-900, GSM-1800 or UMTS band [1].

The most problematic of all the intermodulation distortions are third-order intermodulation products with frequencies $2f_a - f_b$ and $2f_b - f_a$. This is because when the difference between f_a and f_b is small, the intermodulation products fall in-band close to the fundamentals. If the fundamentals at frequencies f_a and f_b are two strong interfering signals, they could produce third-order intermodulation products within the low-noise amplifier of the victim receiver and corrupt the desired signal. The performance metric that characterizes nonlinear devices for such third-order intermodulation products is the "third-order intercept point" (IP3) [2].

In this paper, we use modified model of signal-to-interference-and-noise ratio (SINR) which include the interference due to intermodulation products which could be generated due to receiver nonlinearity. This modified model could be used to analyze receiver nonlinearity characteristic to minimize intermodulation products effect, on the other hand it could be used to modify mobile networks planning technique and frequency allocation algorithms to avoid generating these unwanted interference signals beside of receiver nonlinearity. We use Matlab software to achieve a practical calculations for third-order intercept point (IP3) and effect of intermodulation products on SINR.

II. SINR MODELS

The signal-to-interference-and-noise ratio is defined as the power of a certain signal of interest divided by the sum of the interference power (from all the other interfering signals) and the power of noise all at the output of receiver. In the mobile telecommunication systems standard SINR ($SINR^s$) is widely used to calculate signal-to-interference-and-noise ratio [4] [5] [6].

$$SINR^s = \frac{P_{signal}}{N + P_{interference}} \quad (1),$$

where P_{signal} and N are respectively the desired signal and thermal noise power at the receiver, while $P_{interference}$ is interference power form all external interference resources.

Practically, the most studied interference in the cellular mobile systems are co-channels and adjacent channels interference. This lead to the enhanced SINR model ($SINR^e$) which take into account these two main source of interference.

$$SINR^e = \frac{P_{signal}}{N + \sum_i P_i} \quad (2),$$

where P_i is the power of i^{th} co-channel and adjacent channel interfering signals. The received signal power P_{signal} and P_i could be calculated using one model for signal propagation and path loss. There are many models for co-channel and adjacent channel interference available to use [7] [8].

Standard and enhanced SINR models are used to estimate performance of wireless networks. But these models not

[1]Youssef Abd Alrahman is with the Faculty of Telecommunications at Technical University of Sofia, 8 Kl. Ohridski Blvd, Sofia 1000, Bulgaria, E-mail: tel.eng.josef@live.com.

[2]Ilia Iliev is with the Faculty of Telecommunications at Technical University of Sofia, 8 Kl. Ohridski Blvd, Sofia 1000, Bulgaria, E-mail: igiliev@tu-sofia.bg

considering probability of interference due to nonlinearity of RF receiver. Intermodulation products generated in nonlinear stages in receiver such as mixers and amplifiers could cause interference with the desired signal and therefore should be included.

III. Analysis Of Intermodulation Interference

A. Intermodulation Modeling

Intermodulation products are produced when two or more in-band signals as given in Eq. (3) are applied to the input of a nonlinear receiver has transfer function given in Eq. (4) , these signals mix within the receiver and they form new components that are not harmonics of the input frequencies. These components are termed as intermodulation distortion products, as shown in Fig.1 [2] [9].

$$x = a\cos 2\pi f_a t + b\cos 2\pi f_b t \quad (3).$$

$$y(t) = \sum_{i=0}^{n} k_i * x(t)^i \quad (4).$$

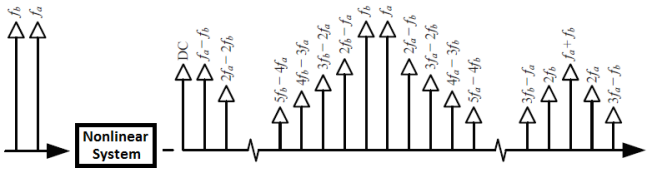

Fig.1. Even and odd-order intermodulation products.

The nth order intermodulation product is given at frequency $\pm n_a f_a \pm n_b f_b \; where \; |n_a| + |n_b| = n.$ The transfer function order could be limited to 3, because the higher order products are of less significance.

In this paper, we consider only the products at frequencies $2f_1 - f_2$ and $2f_2 - f_1$ which are commonly referred as third-order intermodulation distortion (IMD3) products. If the distance between the frequencies of two in-band interferers (f_1 and f_2) is similar to the distance between one of the interferers and the useful signal at f_0, one of the resulting intermodulation products may fall close or within the receiver channel and may corrupt the desired signal. The IMD calculation method based on intercept points is as follow [3]:

When two incoming signals with frequencies at f_1 and f_2 interact, only two third-order intermodulation products of type IM3(2,1) are possible. In case of three signals with frequencies at f_1, f_2 and f_3, intermodulation products of types IM3(2,1) and IM3(1,1,1) are possible. IM3(2,1) and IM3(1,1,1) products frequencies f_{IMD} are as given in Eqs. (5) and (6) respectively.

$$f_{IMD} = 2f_a \pm f_b \quad (5).$$

$$f_{IMD} = f_a \pm f_b \pm f_c \quad (6),$$

where $a, b, c \in \{1,2,3\}$ and $a \neq b \neq c$

Power of intermodulation product IM3(2,1) can be calculated by:

$$P_{IMD-2} = 3(P_{e-in} + G_{RX}) - 2OIP_3 \quad (7),$$

where P_{IMD-2} is output power of the third-order intermodulation product IM3(2,1) in dBm, OIP_3 is 3rd order output intercept point of the receiver in dBm, G_{RX} is receiver gain in dB and P_{e-in} is input power of incoming signal into the receiver in dBm.

$$P_{e-in} = (2P_1 + P_2)/3 \quad (8),$$

where P_1, P_2 are powers of incoming signals at frequencies f_1, f_2 correspondingly. Power of intermodulation product IM3(1,1,1) can be calculated by :

$$P_{IMD-3} = 3\,(P_{e-in} + G_{RX}) - 2OIP_3 + 6 \quad (9),$$

where P_{IMD-3} is output power of the third-order intermodulation product IM3(1,1,1) in dBm. P_{e-in} in this situation is given by:

$$P_{e-in} = (P_1 + P_2 + P_3)/3 \quad (10),$$

where P_1, P_2, P_3 are powers of incoming signals at frequencies f_1, f_2, f_3 correspondingly.The equivalent intermodulation product level recalculated to the input of the receiver P_{in-IMD} (dBm) is equal to:

$$P_{in-IMD} = P_{IMD} - G_{RX} \quad (11).$$

Or it could be calculated by:

$$P_{in-IMD} = 3\,P_{e-in} - 2IIP_3 + 6 \quad (12).$$

Interferences caused by intermodulation products in the receiver occur when the following two conditions are fulfilled:

$$F_R - 0.5B_{IF} \leq f_{IMD} \leq F_R + 0.5B_{IF} \quad (13).$$

and

$$SIR < A \quad (14),$$

where F_R is tuning frequency of the receiver, B_{IF} is passband value of the IF stage or based band filter bandwidth if there is no IF stage and *A* is co-channel protection ratio.

B. Modified SINR model

As shown in Fig.2, intermodulation products create unwanted components at frequencies which may interfere with the desired signal. In a worst case, the IMD3 product will fall directly into the desired channel (similar to co-channel interference). With increasing of the frequency offset between the IMD3 product and the desired signal, their impact to SINR becomes less harmful (similar to adjacent channel interference). Modified model of SINR will include the interference due to third-order intermodulation distortion (IMD3) products and is given by Eq. (15).

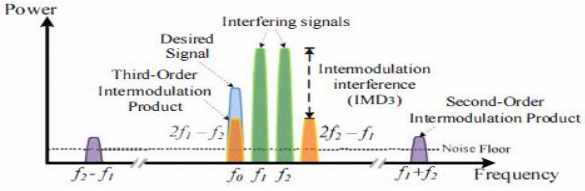

Fig.2. Third-order intermodulation distortion causing interference in the desired channel of a receiver.

$$SINR^m = \frac{P_{signal}}{N + \sum_i P_i + P_{IMD3}} \quad (15),$$

where P_{IMD3} represents interference power caused by third-order intermodulation distortion and it can be expressed by:

$$P_{IMD3} = \sum_k \sum_j P_{IMD-2} + \sum_k \sum_j \sum_l P_{IMD-3} \quad (16),$$

where $k \neq j \neq l$ are the number of frequencies used in the telecommunication system and f_k, f_j, f_l are the signals which produce components with frequency equal to f_{IMD} as given in Eqs. (5) and (6) and this f_{IMD} is achieve the condition in Eq.(13) or it shouldn't be taken into account. In mobile telecommunication systems, there are many ways to minimize interference due to co-channel and adjacent signals during frequency planning such sectoring and cell-splitting and that will increase $SINR^e$ [8] [10]. In this paper we consider interference generated just form intermodulation products, so modified model of SINR can be expressed as:

$$SINR^m = \frac{P_{signal}}{N + \sum_k \sum_j P_{IMD-2} + \sum_k \sum_j \sum_l P_{IMD-3}} \quad (17).$$

IV. Third-Order Intercrept Point IP3 Calculation Using Matlab Software

We calculate third-order intercept point for nonlinear system such as nonlinear amplifier by using simple model as in Fig.3 with two signals with frequencies (990 ,1010 MHz), considering amplifier with gain 0 dB and noise figure 3.01 dB. We use spectrum analyzer at the input and the output of amplifier to measure the power of the fundamental signal and power of third-order product signal.

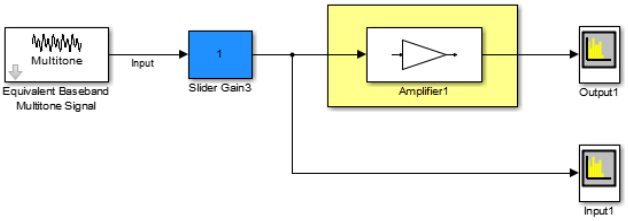

Fig.3. Matlab model for practical calculation.

To achieve that there are two options:

Use two signals at equal level: The power of input signals is equal and range between $(-27 \sim 48)dBm$, by using spectrum analyzers to measure powers at the output, the IP3 could be shown in Fig.4.

Use two signals at different level: Power of the first input signal will be constant at 5 dBm, and the second input signal power will range from $-37dBm\ to\ 49\ dBm$, and with spectrum analyzers measure output powers for the fundamentals signals and third-order intermodulation product. But here to have a correct calculation, the equivalent input and output power are calculated by using Eq. (8). Then by plotting fundamental equivalent signal with third-order intermodulation product, in Fig. 5, could be found that IP_3 is equal to 30 dBm.

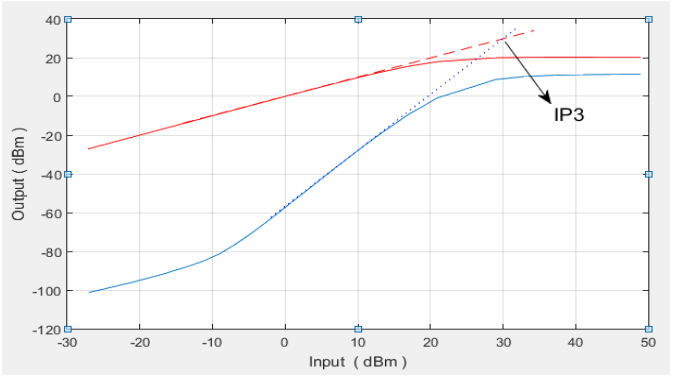

Fig.4. Practical Measurements 1. (blue line for the third intermodulation product)

As shown in Fig.5 the third-order intercept point IP_3 is equal to 30 dBm.

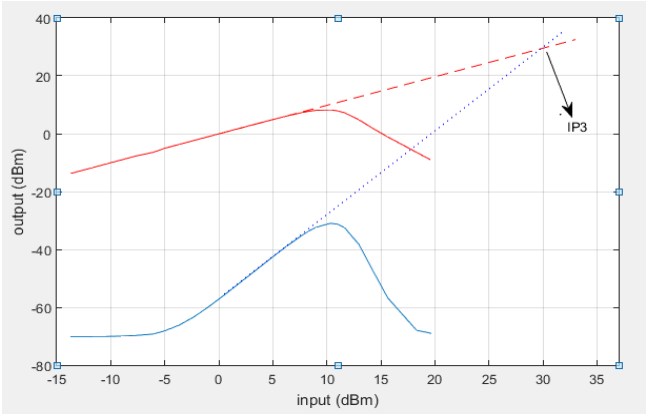

Fig.5. Practical measurements 2. (blue line for the third intermodulation product)

V. Simulation Results Using Modified SINR Model

For GSM receiver with noise floor $N = -111\ dBm$, the minimum SINR value required for GSM receiver is 9 dB. That's mean for desired signal at $-99\ dBm$, if the third-order input intercept point is $IIP = -18\ dBm$ and there are just two interfere signals have intermodulation component at desired signal's frequency, the maximum acceptable power for these signals is $-49\ dBm$ to achieve wanted SINR value [11] [12].

In this simulation, we will examine these conditions for GSM receivers and study the impact of IIP3 and power of interfere signals on SINR according to our modified SINR model using tow interfere signals.

A. Impact of IIP3 on SINR

We use the modified SINR model as expressed in Eq. (17) with GSM receiver specifications from [12]. Fig.6 characterizes relationship between third-order input intercept point IP3 and SINR for different interfere signals power P_{e-in} where desired signal at $-99\ dBm$ and noise floor $-111\ dBm$.

The simulation results are: in term to achieve desired SNR value for RF receivers, the IIP3 should increase with increment of the interfere signals power which may produce intermodulation products in the receiver. As given in [11] [12], third-order input intercept point IIP3 for GSM receiver is about $-18\,dBm$. That's mean when desired signal at $-99\,dBm$ and interfere signals with power more than $-49\,dBm$, SINR will fall under accepted value $-9\,dB$.

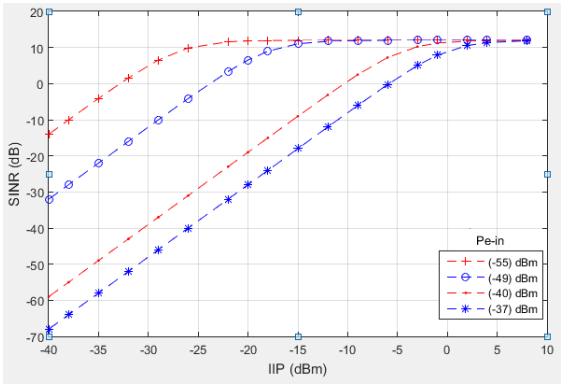

Fig.6. Impact of third-order input intercept point IIP3 on SINR.

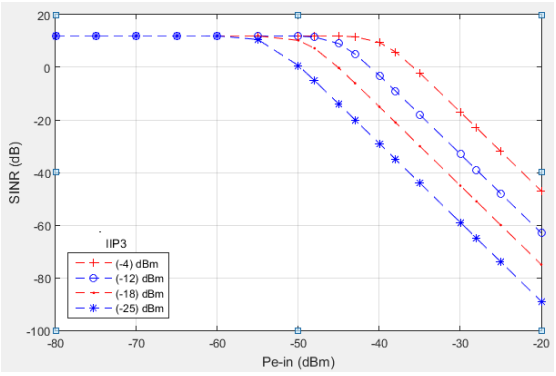

Fig.7. Impact of p_{e-in} on SINR.

B. Impact of interfere signals on SINR

By using our SINR modified model with desired signal at $-99\,dBm$ and noise floor at $-111\,dBm$, relationship between power of interfere signals p_{e-in} and SINR is depicted in Fig.11. To achieve the required SINR for GSM receiver, acceptable interfere signals power is about $-54\,dBm$ when IIP3 is $-25\,dBm$, $-49\,dBm$ when IIP3 is $-18\,dBm$ and about $-40\,dBm$ when IIP3 is $-4\,dBm$. This results show that with increment of the IIP3 value acceptable value for interfere signals power is get increase. From Fig.7, the RF receiver reject for intermodulation products is get higher when IIP3 increase and the linearity of the receiver is increase.

VI. Conclusion

As a result of growth of wireless systems and the existence of many service providers at same area, the intermodulation products distortion rise up as significant issue which should be mitigated to insure required SINR for receivers.

In this paper, we study the effect of third-order intermodulation product on signal-to-interference-and-noise ratio. the results show that when IIP3 increases, the receiver could handle with higher power of interfere signals (producers of third-order intermodulation product) with acceptable value of SINR. Modified SINR model could be used to get control on receiver nonlinearity effect, on the other hand it could be used to modify mobile networks planning technique and frequency allocation algorithms to avoid generating these unwanted interference signals beside of receiver nonlinearity. Thus, there are a lot of challenges for RF receivers designers to achieve all of these requirements.

References

[1] Nuno Borges de Carvalho and Raquel Castro Madureira, "Intermodulation Interference in the GSM/UMTS Bands," , Journal Proc. 3a Conf. de Telecomunicaçoes (CONFTELE 2001), October 2000.

[2] Shabbir Ahmed, " INTERFERENCE MITIGATION IN COLOCATED WIRELESS SYSTEMS," doctoral research, Melbourne, Australia, December 2012.

[3] Rec. ITU-R SM.1134-1, "Intermodulation interference calculations in the land-mobile service," *ITU, 1995-2007.*

[4] Jean-Marc Kelif, Stephane Senecal, Constant Bridon, Marceau Coupechoux, " A Fluid Approach for Poisson Wireless Networks",. Cornell University, New York, USA, January 2014.

[5] Moses Ekpenyong and Joseph Isabona,"AN ENHANCED SINR-BASED CALL ADMISSION CONTROL IN 3G NETWORKS". *International Journal of Wireless & Mobile Networks (IJWMN) Vol. 3, No. 5, October 2011.*

[6] Olga Goussevskaia, Yvonne Anne Oswald and Roger Wattenhofer ," Complexity in Geometric SINR". MobiHoc'07, September 9–14, 2007, Montreal, Quebec, Canada, 2007.

[7] Faramarz Hendesi, Asrar Shiekh and Roshady M.hafiz ," CoChannel and Adjacent Channel Interference in Wireless Cellular Communications". Wireless Personal Communications ,March 2000, Volume 12, Issue 3, pp 239-253.

[8] Nura Muhammad Shehu," Coverage and Capacity Improvement in GSM Network". International Journal of Novel Research in Electrical and Mechanical Engineering, Vol.2 , Issue.3 , pp: 57-62, September-December 2015, [Online].Available: www.noveltyjournals.com.

[9] Q. Gu, RF System Design of Transceivers for Wireless Communications. Springer, 2005.

[10] Lina Lan, Xuerong Gou, Jingli Mao, Wenyuan Ke,"GSM Co-Channel and Adjacent Channel Interference Analysis and Optimization". TSINGHUA SCIENCE AND TECHNOLOGY ISSN 1007-0214 04/12pp583-588 Volume 16, Number 6, December 2011.

[11] Jacques C. Rudell, Jeffrey A. Weldon, Jia-Jiunn Ou, Li Lin, and Paul Gray," An Integrated GSM/DECT Receiver: Design Specifications". UCB Electronics Research Laboratory Memorandum, April 1998.

[12] ETSI TS 100 910 V5.12.0 (2001-02), "Digital cellular telecommunications system (Phase 2+); Radio transmission and reception".[Online].Available: http://www.etsi.org/deliver/etsi_ts/100900_100999/100910/05.12.00_60/ts_100910v051200p.pdf.

Omnidirectional Double Biquad Omni-Antenna for 2.4 GHz Wireless Link Application

Kalina Kalinovska[1] and Peter Z. Petkov[2]

Abstract – **In this paper a modified biquad antenna is proposed. The modified antenna has features, relatively high gain and small physicals dimensions. The directivity is omni in horizontal direction. The antenna is tuned for 2.4GHz-2.45GHz bandwidth. The antenna can be used for Wi-Fi communications and for drones communications.**

Keywords – **Biquad, biQUAD, QUAD, antenna, Omni-antenna, Wi-Fi, drone, omnidirectional**

I. Introduction

The trend in recent years shows that the number of Internet users is increasing and well as the number of devices used by every individual. The realization of user's divices full functionality requires Internet access. More and more devices are mobile and able to connect to the web via a wireless transmission environment. The development of apps that require transmission media is increasing the need of good coverage rapid speed of data transmission over Wi-Fi HotSpots. These Wi-Fi HotSpots are located in different places in our homes, shopping centers, various conference rooms, etc. These antennas should be mostly omni-directed graph with the greatest possible gain. The antennas, which are mainly used for Wi-Fi routers are omni-directed, with a gain of more than 2 dBi, with a minimum vertical width of the radiation pattern. The aim of the article is to develop an antenna for Wi-Fi access by the standards of IEEE 802.11b/g [1], for use in public places that have many users and need antennas with omni-directed radiation pattern. These antennas should provide better coverage in indoor and outdoor environments. Also the aim of article is to prove the ability to use the antenna for communication between the photo-drone and the navigator.

II. Biquad Antenna Concepts

A. IEEE 802.11 standards

IEEE 802.11 is a standard that is used for wireless local area networks (WLAN). 802.11 has several widely used protocol - 802.11a, 802.11b, 802.11g and 802.11n, which are mostly in 2.4 - 2.5 GHz range.

Despite advances in technology standards in 5.25 – 5.35 GHz, 2.4 - 2.5 GHz frequency band is still preferred. 802.11b/g/n [2] standards are preferred over others using higher frequencies. Greater attenuation with higher frequency in free. Development in the article can be used for all standards that are 2.4 - 2.5 GHz frequency band. Through the optimizated model of the current development can be used in different frequency standards.

B. Quad Antenna

Quad antennas are type of loop antenna. These antennas are specific to their closed loop which may have a specific geometric shape. An example is the square loop antenna. The length of each wire is a multiple of the wavelength λ with multiplicity λ / 4. (1.1) (Figure 1) [3]

$$l = \lambda/4 \qquad (1.1)$$

The single square loop antenna has two beams with a maximum gain about 4 dBi. (Figure 2) This antenna is powered by one of its corners. The various loop antennas are preferred for mobile communications at higher frequencies. They also have easy workmanship. Materials for these antennas can come from many places. The conductor of which can produce the antenna can be copper wire. Its thickness can vary depending on the desired bandwidth.

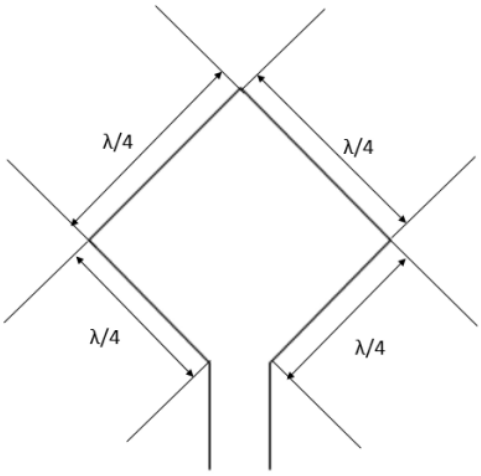

FIG. 1 – QUAD ANTENNA - PRINCIPLED SCHEME

[1] Kalina Kalinovska is a student at Faculty of Telecommunications at Technical University of Sofia, 8 Kl. Ohridski Blvd, Sofia 1000, Bulgaria. kalina.kalinovska@gmail.com

[2]Peter Z. Petkov is with the Faculty of Telecommunications at Technical University of Sofia, 8 Kl. Ohridski Blvd, Sofia 1000, Bulgaria. pjpetkov@tu-sofia.bg

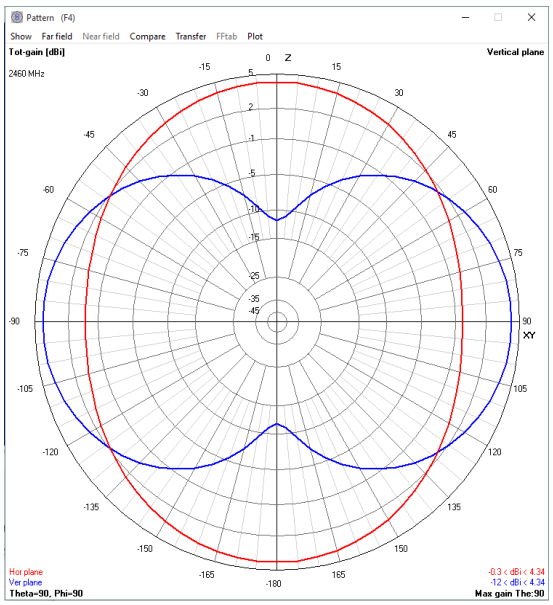

FIG. 2 – QUAD ANTENNA – DIRECTIVITY IN POLAR COORDINATE SYSTEM

C. Biquad antenna

If two square loop antennas join the indicated in (Figure 3), it gets biQUAD antenna. It is easy to construct an antenna which consists of two squares on which can be placed reflector. It provides greater amplification compared to the square loop antenna. The polarization of the emitted signal depends on the spatial location of the antenna. Horizontal - horizontal, vertical - vertical polarization. [4] The horizontal position represents when both squares are next to each other, the vertical position is when both squares are placed one above the other.

The radiation pattern is similar to square loop antenna but biQUAD antenna provides greater gain of almost 5 dBi. The width of the main sheet is approximately 70 degrees. (Figure 4) [5]

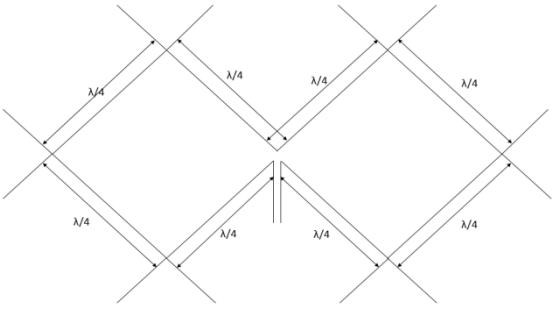

FIG. 3 – BIQUAD ANTENNA – PRINCIPLE SCHEME

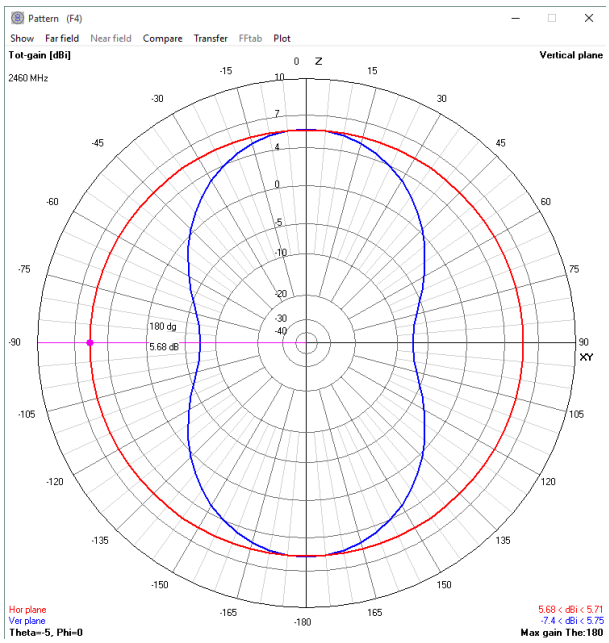

FIG. 4 – BIQUAD ANTENNA – DIRECTIVITY PATTERN IN POLAR COORDINATE SYSTEM

D. Double Biquad

When connecting two Biquad antennas, as described in Figure 5 scheme gets Biquad. The antenna is with horizontal omni-directional radiation pattern. (Figure 6) This type of antennas are not widespread. In recruiting literature examination of the problem were not found formulas and previous developments. The theoretical data comparable and similar structures show that each side of it must have a length of λ/4, but the simulations and practical measurements do not match the theoretical model. When optimizing antenna simulation with 4nec2 software, there is a tendency in extending the wires. In real conditions there is an extension of the wires by ~20%. The prototype (Figure 6) confirmed these simulations.

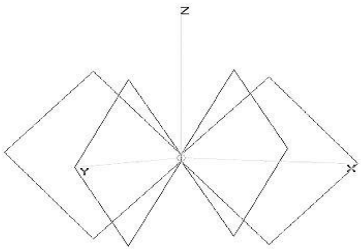

FIG. 5 – DOUBLE BIQUAD ANTENNA – PRINCIPLED SCHEME

This extension is due to surface currents distribution on the wires and the angle between the wires. The directivity of the antenna is omni in bough horizontal and vertical direction (Figure 6)

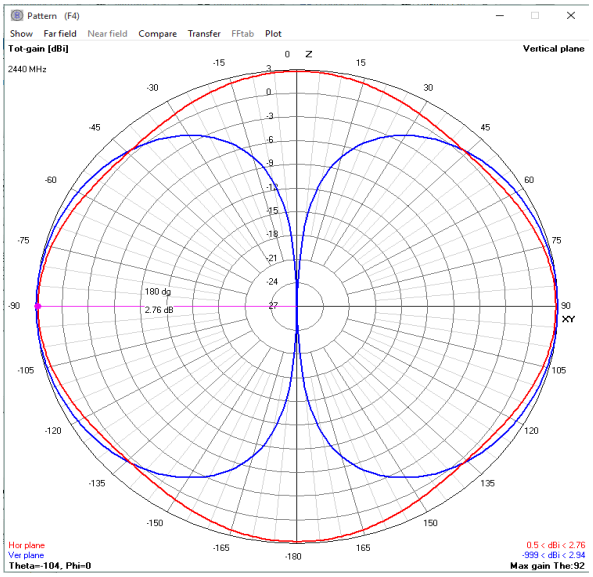

FIG. 6 – DOUBLE BIQUAD ANTENNA – DIRECTIVITY IN POLAR COORDINATE SYSTEM

The simulation model showed bandwidth is 2200-2700MHz . The prototypes bandwidth is wider than the theoretical model (Figure 7).

The prototype of the antenna was made from copper wire with thickness of 2mm and SMA female connector. The center frequency was shifted because of the complicated geometric shape.

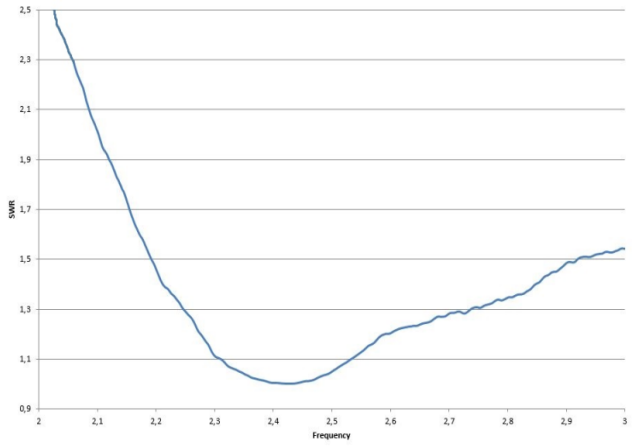

FIG. 7 – DOUBLE BIQUAD ANTENNA – PROTOTYPES BANDWIDTH, SWR, EXPERIMENTAL MEASUREMENTS

E. Double biquad with reflector

When placing a reflector at a distance of λ/4 from the center of the structure. (Figure 8) The antenna with reflector is not omni in vertical direction, but in horizontal is. The maximum gain is 4.5dBi. (Figure 9, Figure 10) Reflector can be placed below the antenna. The best position is λ/4 from the geometrical center of the structure.

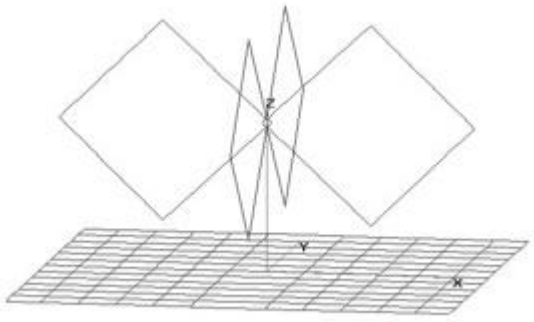

FIG. 8 – DOUBLE BIQUAD ANTENNA WITH REFLECTOR– PRINCIPLED SCHEME

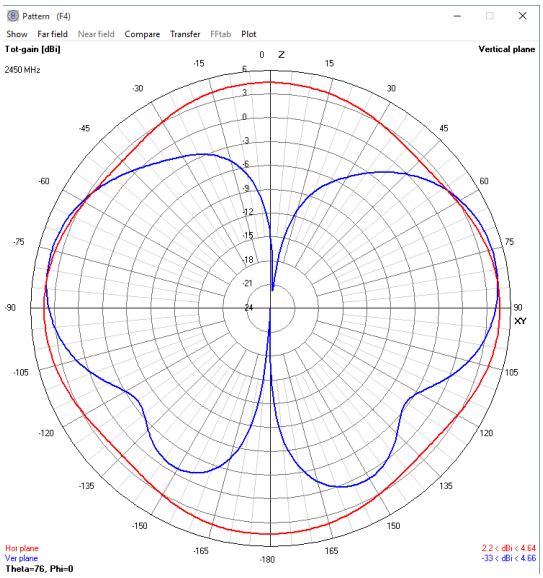

Fig 9 – Double biquad antenna with reflector– directivity in polar coordinate system

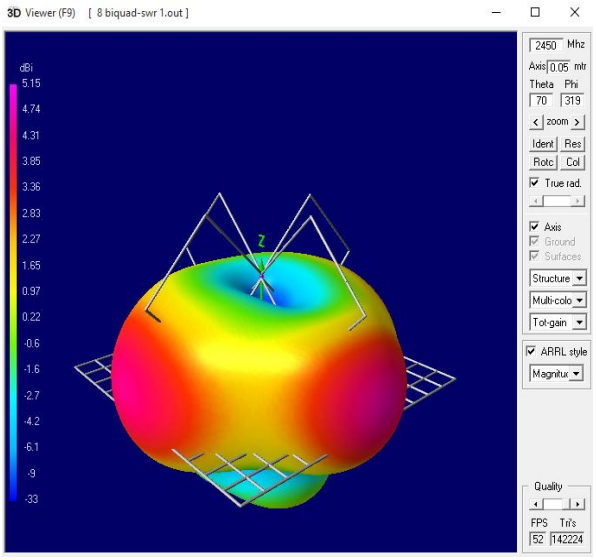

FIG. 10 – DOUBLE BIQUAD ANTENNA WITH REFLECTOR – DIRECTIVITY IN 3D

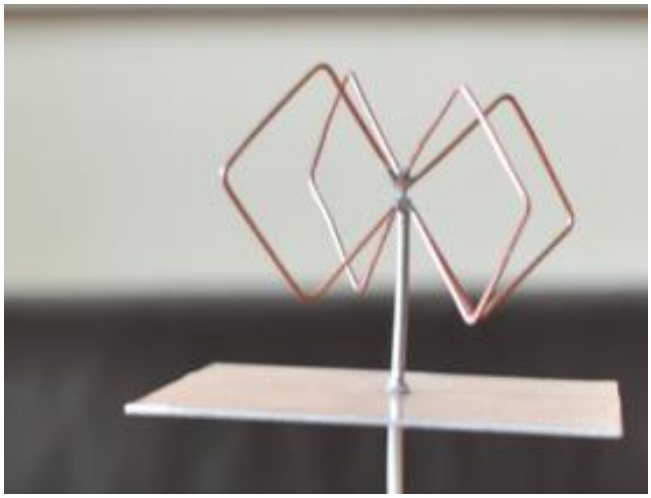

FIG. 11 – BIQUAD ANTENNA WITH REFLECTOR – PROTOTYPE

The simulation model showed bandwidth is 2350-2700MHz. The prototypes bandwidth is wider than the theoretical model (Figure 12). That can be explained with the non-idealistic characteristics of the copper wire that was used for the prototype. The prototype has higher gain then the antennas that are used in middle and low-cost Wi-Fi routers. The antenna can be placed upside-down on a sealing for better coverage in shopping centers and conference halls.

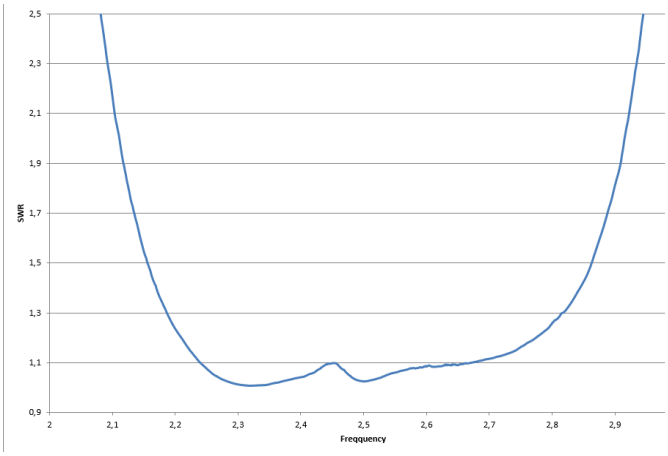

FIG. 12 – BIQUAD ANTENNA – PROTOTYPES BANDWIDTH, SWR, EXPERIMENTAL MEASUREMENTS

III. CONCLUSION

A modified double biquad antenna with reflector has been developed and examined in this study. The article shows a new type of loop antenna, modified with reflector. Double biquad antenna with reflector has the highest gain from every other simulation of QUAD type antennas (Table 1). Modified double biquad antenna with reflector shows satisfactory electrical performance, compact size and easiness to manufacture, which makes it a strong candidate for practical applications. It can be used as standalone antenna and in different arrays, depending of the specifical structure of a building. The innovative approach chosen for antenna modification can lead to future developments in this still relatively undeveloped area of antenna design.

TABLE 1
COMPARATIVE ANALYSIS

Type of the antenna	Gain	Directivity in horizontal direction	Conclusion
Quad	2 dBi	Dipole type	It is not relevant to the task
Biquad	2 dBi	Dipole type	It is not relevant to the task
Double biquad	2 dBi	Omni	It is not relevant to the task
Double biquad with reflector	4.5 dBi	Omni	The directivity is

REFERENCES

[1] "IEEE-SA Standards Board Operations Manual". *IEEE-SA*. Retrieved 2015-09-13.

[2] ARRLWeb: Part 97 - Amateur Radio Service". American Radio Relay League. Retrieved 2010-09-27

[3] Hall, Gerald (1991). The ARRL Antenna Book (15th edition). ARRL. p. 24. ISBN 0-87259-206-5.

[4] evelaqua, Peter J. "Types of Antennas". Antenna Theory. Antenna-theory.com Peter Bevelaqua's private website. Retrieved June 28, 2015

[5] Johnson, R, Jasik, H, ed. (1984). Antenna Engineering Handbook. McGraw Hill.

Synthesis of Wideband Edge Coupled Microstrip Filters with Defected Ground Structures

Marin Nedelchev, Alexander Kolev, Ilia Iliev[1]

Abstract – **The paper presents design, simulation and measurement of an edge coupled microstrip filter with a dumbbell type defected ground structure (DGS). For the design purposes, the coupling coefficients of the coupled resonators with defected ground structure were investigated using full wave electromagnetic simulator. The design graphs for the coupling coefficient used for the filter synthesis are presented. Based on the simulation results a five pole filter with a Chebyshev response was simulated, manufactured and measured. There is a very good agreement between the simulation and the measured results.**

Keywords – **microstrip coupled, resonator, coupling coefficient, defected ground, dumbell**

I. INTRODUCTION

The emerging communication systems, allow users to communicate at ever higher speeds, which result in stringent requirements on the increase of bandwidth in which the devices have to operate. Filters play an important role in many microwave applications. But the filter response requirements become more stringent to the insertion loss, wider bandwidth, and steeper response in the stopband. In most cases the microstrip filters are designed using Chebyshev approximation.

The main problem designing wideband and ultrawideband coupled resonator filters are the tight gaps between the resonators. Then the manufacturing tolerances have serious impact on the coupling coefficients and the filter's response. One of the possible solution of this problem is using interdigital or combline filters, but their common drawback that they require a short circuit in microstrip technology. Another possible solution is using etched topologies in the ground plane of the microstrip, known as defected ground structures in edge coupled halfwave filter. This filter is proposed by S. Cohn in his famous paper [11]. It is preferred by the designer because of its clear theoretical and practical design procedure, easy adjustment, descent performance in the stopband and relatively large size in the lower GHz band. The realizable relative bandwidth of the filter is between 5 and 35%.

DGS is realized by introduction of a topology etched in the ground plane of microstrip as shown on Fig.1 [9]. It disturbs the shielded current distribution depending on the shape and dimension of the defect. The disturbance at the shielded current distribution will influence the input impedance and the current flow of the microstrip lines. The positions and lengths of the dumbbell sections control the response and insertion loss of the designed device. DGS increases the effective values of dielectric constant of substrates (ε_{eff}) , thus, decreases the wavelength and the overall length of the design.

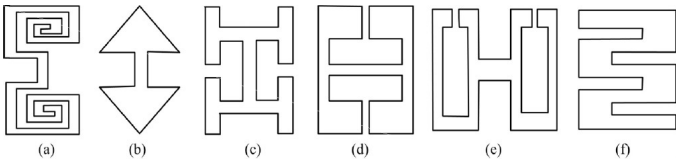

Fig.1 Types of DGS elements-(a) spiral head, (b) arrowhead-shot, (c) "H"-shape slot, (d) a square open-loop with a slot in middle section, (e) open-loop dumbbell and (f) interdigital DGS

Defected ground structures has many practical applications in microwave planar devices. They can be applied in the design of microstrip filters, microstrip antennas, power dividers, matching networks. The main effects connected to introduction of DGS are size reduction of the device [5], harmonic control [4], sharp rejection and wide stopband[2], better matching of the feed lines [6]. It is shown in [1] that the DGS can improve and control the radiation property of microstrip antenna and suppress the cross-polarized radiation from microstrip array [7].

Introduction of DGS in coupled resonator microstrip filters can increase the bandwidth and to cause multiband response. This is the reason to investigate in more details the possibilities of design of wideband microstrip filter using DGS.

The coupling enhancement scheme is based on the difference between the dielectric constants in even and odd modes of the coupled lines. The defected ground structure can control the effective dielectric constant. In even mode, the wave travels longer way and the signals slow down. In that case the phase velocity for even mode decreases. Therefore, the effective dielectric constant increases. In odd mode E-field pattern is asymmetric i.e., E-field is continuous even in presence of a DGS. So the signal path in odd mode is exactly the same as without a DGS. Hence waves do not experience any slow-wave effect and thus the dielectric constant for odd mode remains unchanged. Therefore, the overall effective dielectric constant increases with the inclusion of a DGS and thus, the coupling coefficient enhances [3,8].

This paper presents a synthesis procedure of wideband edge coupled halfwave microstrip resonators with a dumbbell type defected ground structure. The procedure follows the Chebyshev approximation and calculation the coupling

[1]Marin Veselinov Nedelchev, Alexander Kolev and Ilia Iliev –are with Dept. of Radiocommunication and Videotechnologies in Faculty of Telecommunication in TU –Sofia, N8, Kliment Ohridski bul., 1700 Sofia, Bulgaria. E-mail: mnedelchev@tu-sofia.bg

coefficient between the resonators. A fullwave planar EM simulator is used in order to obtain the corresponding coupling coefficients. The synthesized filter is simulated, manufactured and its frequency responses are measured. There is a very good agreement between the simulated and measured results.

II. HALFWAVE COUPLED RESONATOR WITH DUMBBELL TYPE DEFECTED GROUND STRUCTURE

All the simulations, design procedures in the paper are performed for dielectric substrate FR-4 with height 1.5mm, relative dielectric constant $\varepsilon_r=4.4$ and loss tangent $tg\delta=0.02$.

The form of the dumbbell type defected ground structure and its dimensions is shown on Fig. 2. It consists of a main slot connected on both ends to rectangular dumbbell heads.

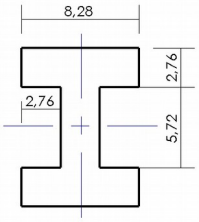

Fig.2. Form and size of the DGS (all sizes in mm)

The edge halfwave coupled resonators have width corresponding to the width of a line with a characteristics impedance of 50Ω. For the dielectric substrate FR-4, it is computed that the width of the line is $w=2.76\,mm$.

Fig.3 shows two coupled resonators with length l=32.82mm for center frequency $f_0=2.4\,GHz$. The length is determined using a simulation in a full wave EM simulator.

Fig.3 Two coupled resonators with length 32.82mm and width 2.76mm

Fig.4 shows two coupled resonators with length l=32.82mm for center frequency $f_0=2.4\,GHz$ with the DGS shown on Fig.2 in the ground plane.

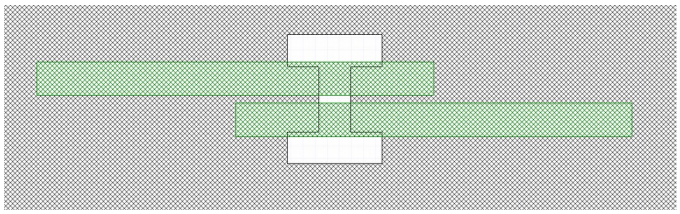

Fig.4 Two coupled resonators with length 32.82mm and width 2.76mm with DGS in the ground plane

The corresponding coupling coefficient for synchronously tuned resonators can be calculated easily by the resonance frequencies of even and odd mode [10], when the coupled resonators are overcoupled:

$$k=\frac{f_e^2-f_0^2}{f_e^2+f_0^2} \tag{1}$$

A full wave EM simulator based on the Method of the Moments (MoM) is used to identify the resonance frequencies in the response. Figure 5 shows the calculated coupling coefficient of the coupled resonators, when there is no DGS and when we place a dumbbell DGS with the form and dimensions shown in Fig.4.

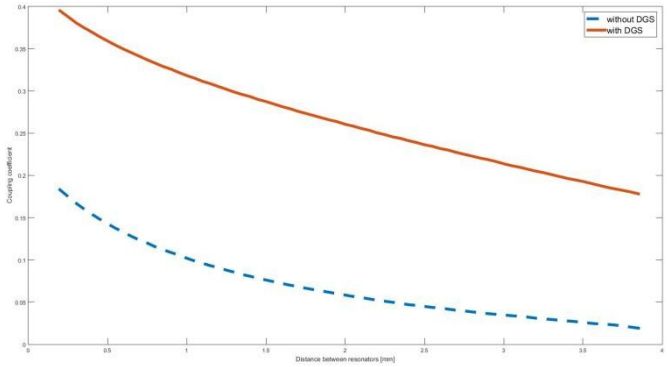

Fig.5 Coupling coefficient between halfwave resonators with (dashed line) and without DGS (solid line)

III. DESIG OF A WIDEBAND EDGE COUPLED FILTER WITH DGS

The designed filter will have a frequency response based on the Chebishev approximation of the 5 order. Therefore the required coupling coefficients must be computed using [10]

$$k_{n,n+1}=\frac{FBW}{\sqrt{g_n\cdot g_{n+1}}} \tag{2}$$

Where FBW is the fractional bandwidth and $g_n \quad n=0-5$ are the values of the element of the lowpass fiter prototype. There are various sources of precomputed values for the elements for different pass band ripple. The current design uses $L_r=0.1\,dB$ and the values for the elements [10] are

$$g_0=g_6=1$$

$$g_1=g_5=1{,}1468$$

$$g_2=g_4=1{,}3712$$

$$g_3=1{,}9750$$

The needed coupling coefficient are computed using (2) and are

$$k_{0.1}=k_{5.6}=0.19563$$

$$k_{1,2}=k_{4.5}=0.16707$$

$$k_{2,3}=k_{3,4}=0.12731$$

Next step is to determine the needed separation between the edge coupled resonators. This is done using a full wave EM simulator and extracting the coupling coefficient when the resonators are overcoupled. After a parametric study of the DGS the extracted separation between the resonators are as follows

$$s_{0,1}=s_{5,6}=0.7\,mm$$

$$s_{2,3}=s_{4,5}=1.05\,mm$$

$$s_{3,4}=1.75\,mm$$

For comparison without the DGS etched in the ground the plane the distances between the resonators has to be

$$s_{0,1}=s_{5,6}=0.13\,mm$$

$$s_{2,3}=s_{4,5}=0.30\,mm$$

$$s_{3,4}=0.65\,mm$$

It is obvious how much the separation between the resonators can be increased then a DGS are inserted under the coupled lines of the filter.

Based on the previous calculation the resulted microstrip edge coupled coupled filter is shown on figure 5 a). Figure 5 b) depicts the filter after tuning with an EM simulator.

Figure 6 show the simulated return loss and insertion loss of the designed filter

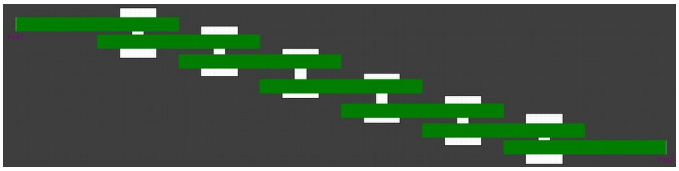

a)

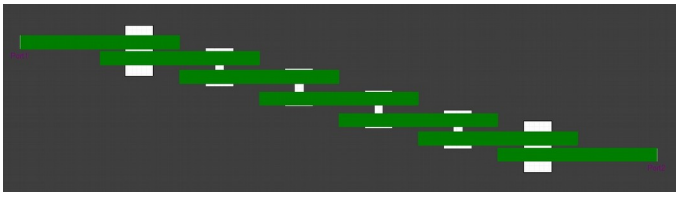

b)

Fig 5 Topology of the designed filter a) based upon calculation b) tuned using a electromagnetic simulator

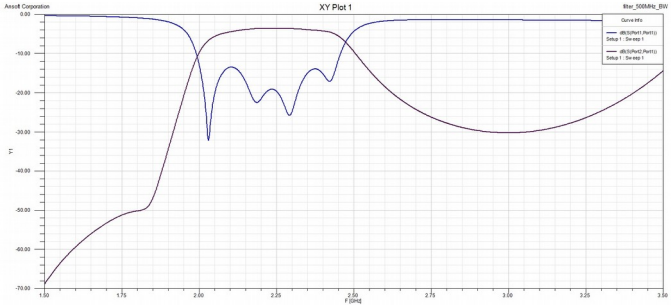

Fig.6 Simulated frequency response of the return loss and inserted loss.

After simulation the filter was fabricated. Figure 7 depicts a top and bottom view of the manufactured filter.Afterwards the return loss and the inserted loss of the manufactured filter ware measured. The measurements are shown on figure 8.

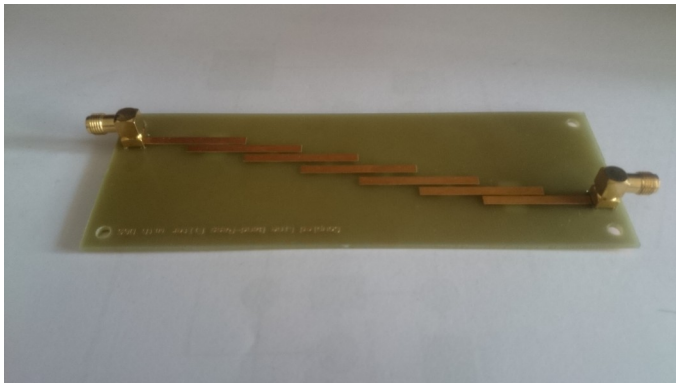

a)

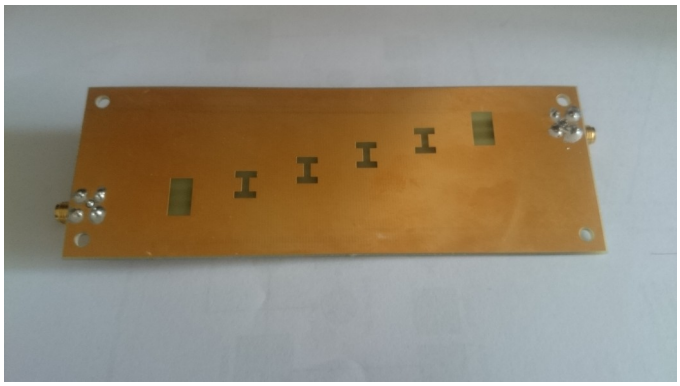

b)

Fig. 7 Top a) and bottom b) side of the manufactured filter.

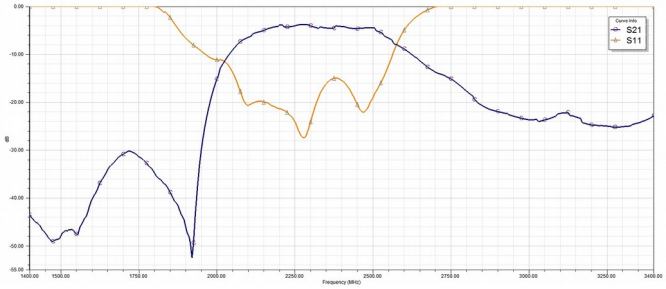

Fig.8 Measured return loss /S11/ and inserted loss /S21/

IV. Conclusion

This paper presents the procedures for designing a wideband edge coupled filter using DGS. The filter was designed according to the Chebishev approximation. A full-wave electromagnetic simulator was used to extract the required distances with regards to the coupling coefficients and to model the frequency response of the designed filter. The modeled filter was produced and the measured results are in good agreement with the ones acquired from the EM simulator.

REFERENCES

[1] F.Y. Zulkifi, E.T. Rahardjo and D.Hartanto, “Radiation Properties Enhancement Of Triangular Patch Microstirp Antenna Array using Hexagonal Defected Ground Structure”, Progress In Electromagnetics Research M, Vol. 5, 101-109,2008.

[2] Ke LU, Guang-Ming WANG, He-Hiu XU, "Compact and Sharp-Rejection Bandstop Filter Using Uniplanar Double Spiral Resonant Cells", Missle Institute of Air Force Engineering University, Sanyuan, Shaanxi, China.

[3] Si-Si Chen, Lin Li and Zhi-Yong Chen, “A Novel Coupled-Defected Ground Structure with Enhanced Coupling-Coefficient and Its Application in Filter Desing”, Progress In Electromagnetics Research Letters, Vol. 52, 93-97, 2015

[4] R.A. Pandhare, P.L. Zade and M.P. Abegaonkar, ”Harmonic Control by Defected Ground Structure on Microstrip Antenna Array” Indian Journal of Science and Technology, Vol.8 (35), December 2015

[5] R.A. Pandhare, P.L. Zade and M.P. Abegaonkar “Miniaturized Microstrip Patch Antenna Arrat at 3.8 GHz for WiMax Application” IOSR Journal of Electronics and Communication Engineering, Volume 10, Issue 6, Ver.I, (Nov-Dec, 2015),PP 20-24

[6] S.Kakkar, A.P. Singh and T.S. Kamal, “Application of DGS in Microstip Patch Antenna”, International Journal of Computer Applications (0975-8887), International Conference on Advancements in Engineering and Technology 2015

[7] D. Guha, C. Kumar and S.Pal, “Improved Cross-Polarization Characteristics of Circular Microstrip Antenna Employing Arc-Shaped Defected Ground Structure”, IEEE Antennas and Wireless Propagation Letters, Vol.8, 2009

[8] N. Militaru, M.G. Banciu and G.Lojewski, “Enhanced Couplings in Broadband Planar Filters with Defected Ground Structures”, Romanian Journal of Information, Science and Technology Volume 10, Number 2, 2007, 199-212

[9] L.H. Weng, Y.C.Guo, X.W. Shi and X.Q.Chen, “An Overview on Defected Ground Structure”, Progress In Electromagnetics Research B., vol. 7, pp. 173-189, 2008.

[10] J.Hong, M.J Lancaster, "Microstrip Filters for RF/Microwave Applications", John Wiley and Sons Inc, 2001.

[11] S. B. Cohn, “Parallel Coupled Transmission LineResonator Filters,” Microwave Theory and Techniques, IRE Transactions on , vol. 6,no. 2, pp. 223-231, April 1958

Modified Fractal Super J-pole Antenna

Boncho Bonev[1],Peter Petkov[2] and Nina Spassova[3]

Abstract – **In this paper a super J-pole antenna with two modified fractal Koch curve shaped elements is proposed. In order to increase the bandwidth and to provide proper phasing of the currents in the antenna elements, the length of some elements of the fractal has been changed. The antenna performances (radiation patterns, VSWR and gain) are simulated and optimized for GSM-1800, UMTS-2100 and Wi-Fi 2,4 GHz bands. Proposed Koch curve super J-pole antenna features relatively small size and high gain.**

Keywords – **Super J-pole, Fractal, Koch curve, Wideband, Multiband.**

I. Introduction

One of the biggest problems in wireless communications is the design of the antennas. They should work in wide frequency band while being small physically. The rule in such cases, as states in [1] is that the bandwidth of an antenna enclosed in a sphere of radius r can be improved only if the antenna utilizes efficiently, with its geometrical configuration, the available volume within the sphere. Several antenna types meet this requirement and fractal antennas are one of them [2-4]. They bear such name after the concept of fractals.

In our previous works [5,6] these concepts have been presented on other types of fractal antennas - research on fractal antennas performance, fractal antennas for some specific applications - Wi-Fi hotspots, digital TV reception, etc. In this paper are proposed and analyzed a super J-pole modified fractal antenna based on Koch curve. This approach represents a wideband and multiband performance, acceptable total gain and relatively small size. The main antenna parameters - radiation pattern, return loss and antenna gain were simulated.

II. Theoretical Analysis

A. J-pole and Super J-pole Antenna

The J-pole antenna (Fig. 1) is an omnidirectional antenna, so called because of its similarity with the letter "J". It is formed by a vertical half-wavelength radiator end-fed by a quarter-wavelength matching stub. One of the advantages of this antenna comes from the fact, that the lower end of the matching stub can be used for direct grounding. The impedance matching of the J-pole antenna is achieved by moving the feed point between the radiator and the stub short, back and forth, until point where they resonate with the transmitter frequency is reached[7,8].

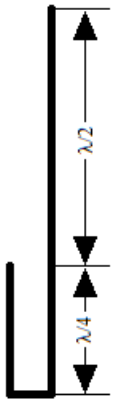

Fig. 1. J-pole antenna

When designing a J-pole antenna there are several particularities that should be taken into account [2]. First of all to achieve negligible radiation from the matching stub, the spacing between its two conductors must be commensurable with the wavelength. The current in the two parallel lines must be with phase difference of 180º and of course the open end of the stub must have infinite impedance while the connected one should be very high, but not infinite.

The Super J-pole antenna (Fig. 2) is a variation of the J-pole. It still has the basic construction of the J antenna, but also has an additional half-wavelength radiator which is connected to the first one with a quarter wave-length phasing stub. The phasing stub is used to unify the phases of the currents in the two radiators. This type of antenna provides more gain compared to the classical J-pole version.

The design of the Super J-pole antenna doesn't differ very much from the J-pole's. Same conditions, mentioned above, must be met to obtain the maximum performance from this antenna construction. Also the space between the two collinear radiators should be very small in order to derive the biggest profits of their collinear placement.

B. The Koch curve fractal

Geometrical figures which are formed by miniaturized identically scaled copies of themselves are called fractals. The operation used to obtain their form is iteration – endlessly repetition of certain steps. The more times we do these steps, the more accurate the fractal will be, but also it will become more complex [3].

[1]Boncho Bonev is with the Faculty of Telecommunications at Technical University of Sofia, 8 Kl. Ohridski Blvd, Sofia 1000, Bulgaria, E-mail: bbonev@tu-sofia.bg.

[2]Peter Petkov is with the Faculty of Telecommunications at Technical University of Sofia, 8 Kl. Ohridski Blvd, Sofia 1000, Bulgaria. E-mail: pjpetkov@tu-sofia.bg.

[3]Nina Spassova is with the Faculty of Telecommunications at Technical University of Sofia, 8 Kl. Ohridski Blvd, Sofia 1000, Bulgaria.

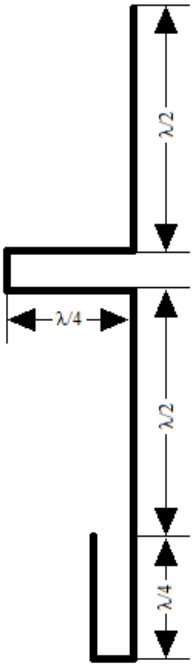

Fig. 2. Super J-pole antenna

One of the fractals used in antenna theory and design to miniaturize the antenna elements and help utilize the frequency band more efficiently is the Koch curve. To form it we start with a straight line, initiator, and split it into three equal parts. After that we build an equilateral triangle over the middle part and remove its foundation (the middle section of the line) - first iteration (n=1) in Fig.3. We do the same thing with the remaining two sides of the triangle and the two parts of the initiator, as shown below to obtain the 2-nd order Koch curve - n=2. We can continue these steps to obtain a fractal with the desired form, precision and complexity.

The total length of the Koch curve can be given with equation [4]

$$L = L_0\left(\frac{4}{3}\right)^n, \qquad (1)$$

where L_0 is the 0-th order length, also called initiator, and n is the iteration number.

III. Design and Simulations

As initial step a super J-pole antenna is designed using a known calculation approach [2]. The two elements of the antenna is shaped as 1-st order Koch curve. Then the length of the elements in two triangle parts of each radiator of the antenna has been changed to provide the proper phasing of the currents in the antenna elements. The optimizations and simulations of antenna parameters (VSWR and antenna peak gain) are performed with 4nec2 moments-method software (www.qsl.net/4nec2) for the frequency band 1,71-2,49 GHz. The simulated and optimized antenna model is presented on

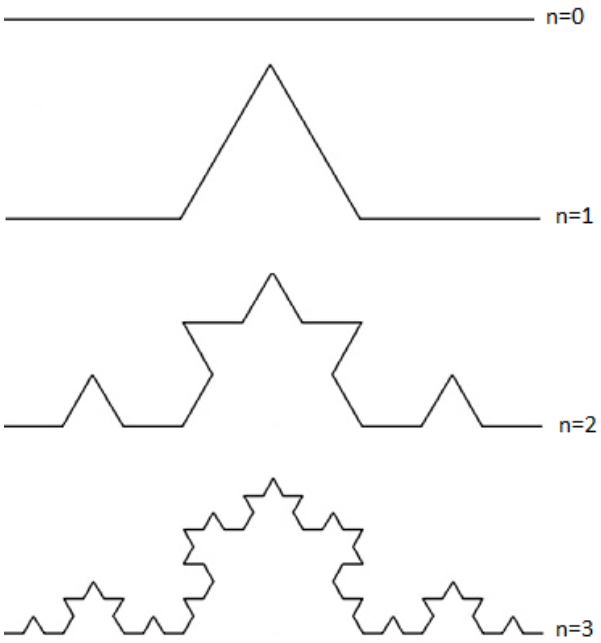

Fig. 3. Generation of the Koch curve

Fig. 4 and the elements length in mm are given in Table I. The antenna elements are round wires with radius 1.75mm.

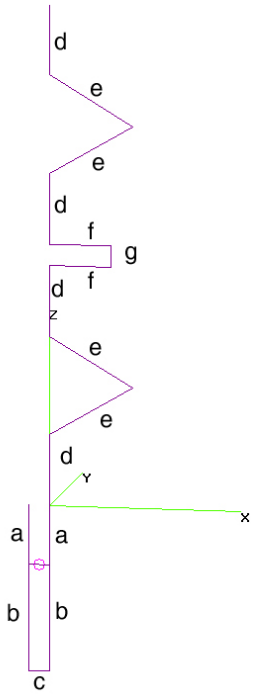

Fig.4. Proposed design of super J-pole fractal antenna

TABLE I
ANTENNA ELEMENTS LENGTH

a	b	c	d	e	f	g
30	54	11	36	50	32	11

In simulations up to 200 segments per half wave length are used which provides the necessary accuracy of the simulations.

The proposed antenna has two frequency bands of operation where the VSWR is lower than two (see Fig. 5 and Fig. 6). The first one (Fig. 5) is from 1.735 GHz to 2.52 GHz and the second one (Fig. 6) is from 4.785 GHz to 5.125 GHz. The bandwidth for the 1-st frequency band is 37,4 % and 6,9 % for the 2-nd one for the proposed fractal antenna while the classical antennas (non fractal) in most cases has not usable 2-nd frequency band of operation.

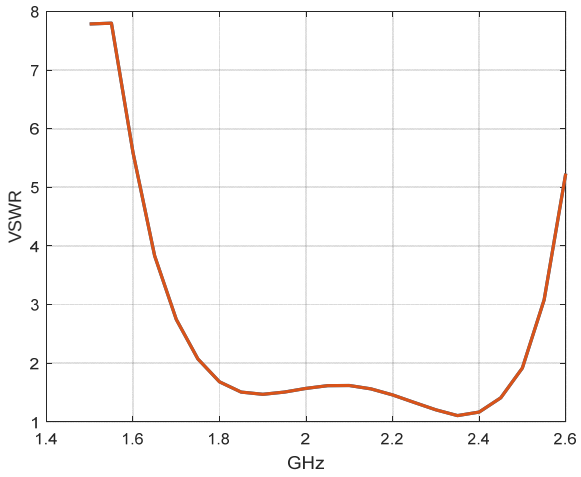

Fig. 5. Simulated VSWR for 1-st frequency band

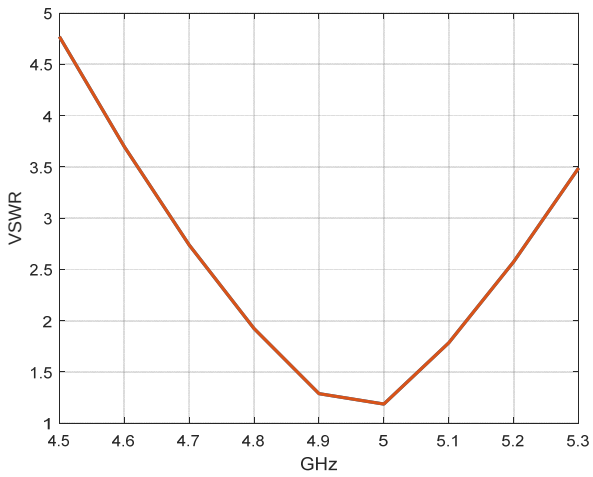

Fig. 6. Simulated VSWR for 2-nd frequency band

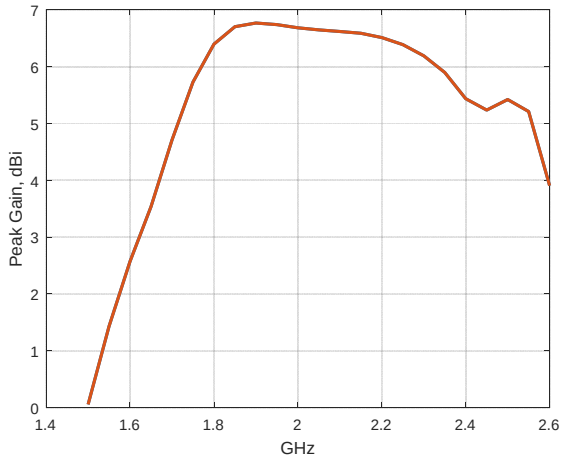

Fig. 7. Simulated antenna peak gain for 1-st frequency band

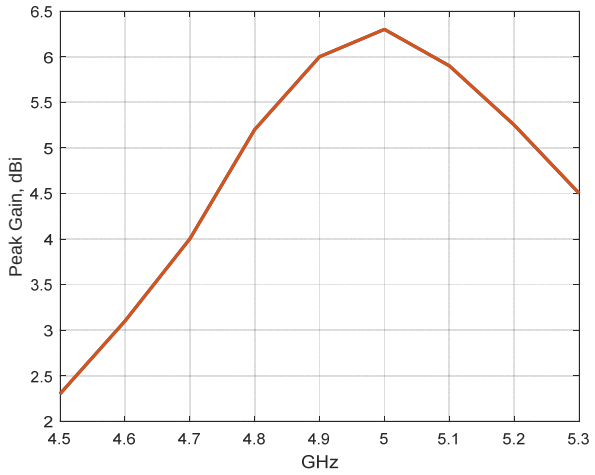

Fig. 8. Simulated antenna peak gain for 2-nd frequency band

The peak antenna gain for both bands of operation is displayed on Fig. 7 and Fig. 8. It is noticeable that the gain easily exceeds 5.2dBi, which is almost the maximum achievable with a single wire antenna. The maximal gain for first operation band is 6.8dBi and for the 2-nd one is 6.3dBi. It is obvious that the peak gain stays relatively constant.

In other hand the antenna shows directional properties (Fig.9 and Fig.10), because of the specific current distribution, especially in the upper band.

It has almost omnidirectional horizontal radiation pattern for the lower band of operation and directional vertical pattern. In the vertical plane, the antenna acts as a linear antenna array formed by several dipoles. The phasing section and fractal elements length modification provides a proper phase shift in a large frequency band, therefore the vertical pattern doesn't vary a lot with the frequency.

For the upper frequency band the antenna construction acts also as linear array, however the identical phase distribution of the currents is provided by more not tightly controlled manner (i.e not optimized).

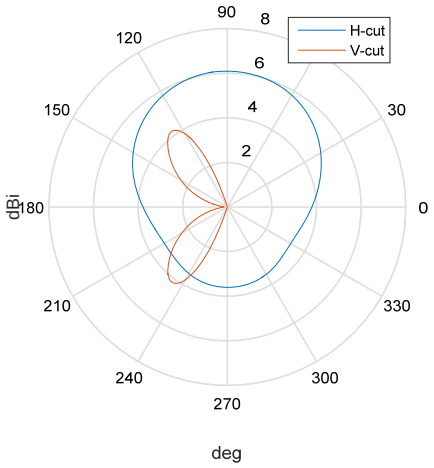

Fig. 9. Simulated radiation patterns for 2GHz.
(Z-axis of the antenna is aligned with 180-0 deg line)

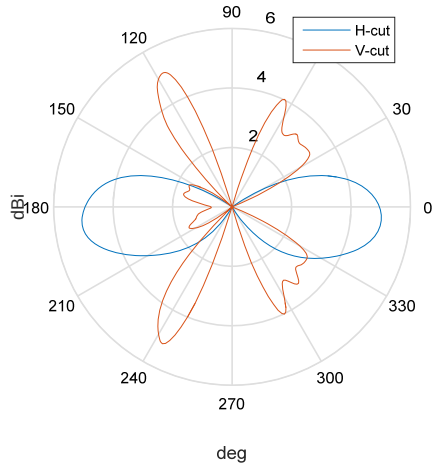

Fig. 10. Simulated radiation patterns for 5 GHz.
(Z-axis of the antenna is aligned with 180-0 deg line)

IV. Conclusion

A fractal super J-pole antenna with radiation elements shaped as Koch curve is introduced in this paper. Fractal shape is used in order to reduce antenna size and to achieve the multiband performance. For increasing the main operation frequency band fractal elements with different length is used. In this case the 37.4 % frequency band is achieved. The second advantage of the proposed fractal antenna is the dual-band performance.

With additional frequency tuning the proposed antenna can be used, among many others, for cellular repeaters - GSM 1800, UMTS 2100, Wi-Fi hotspots, etc.

References

[1] C. Balanis, “Antenna theory” (Third edition), John Wiley& Sons, 2005.

[2] E. A. El-khouly, H. A. Ghali, "High Gain Fractal Based Antenna", Proc of Antennas and Propagation Conference 2008, Loughborough, United Kingdom, pp. 405-408, March 2008.

[3] Balanis, C., “Modern antenna handbook”, John Wiley & Sons, 2008

[4] M. N. A. Karim , M. K. A Rahim, M. Irfan, T. Masri, "Fractal Koch Curve for UHF Band Application", Asia-Pacific Conference on Applied Electromagnetics - APACE 2007, pp. 1-4, December 2007.

[5] P. Petkov, M. Kolev, B. Bonev, "Fractal Yagi Antenna", 2015 Conference of Microwave Techniques (COMITE), pp. 1-3, Pardubice, Czech Republic, April 2015.

[6] P. Petkov, B. Bonev, “Analysis of a Modified Sierpinski Gasket Antenna for Wi-Fi Applications”, Proc. of 24th International Conference RADIOELEKTRONIKA’2014, pp. 1-3, Bratislava, Slovak Republic, April 2014.

[7] Beggerow, Hans (1909). "Zeppelin Antenna" (PDF)

[8] Richardson, D. (K6MHE) “The J-Pole Revisited”, CQ Magazine, pp 34-41, March 1998.

Experimental Determination of 2biQUAD Antenna Radiation Pattern Using CRM Method

Kalina Kalinovska[1] and Kliment Angelov[2]

Abstract – **In this article was made experimental determination of radiation pattern to 2biQUAD antenna with reflector, designed for untargeted applications in ISM bands. An interest in the article is the radiation pattern in vertical direction. The results of this type of measurements can be used to provide radio coverage for different radio networks.**

Keywords – **2biQUAD, radiation pattern experimental mesurments, antenna, Omni-antenna,**

I. INTRODUCTION

In today's world of unlimited communication options are available many technologies using radio signals. They are providing coverage to subscribers with relevant services, while giving the opportunity to be mobile. Examples of such technologies are mobile cellular networks of second and third generation, Wi-Fi, WiMAX and others. Parallel to that the radio communications are used in different technologies for access control, RFID and others using radio signals in the ISM bands. The transmission of information in all of these technologies is made by providing radio in separate zones, aiming at the optimum use of radio resources. For example, Wi-Fi is using different access points (HotSpot), served by antennas that can be with narrow radiation pattern beam or with omni-directional radiation pattern. The directivity of the antenna must be appropriate to comply with the necessary radiation pattern and consistent with the structure of the building that the Wi-Fi coverage will be developed.

Solution for shopping centres and conference halls with many Wi-Fi users is 2biQUAD antenna with reflector. It can realize relatively uniform radiation pattern in a horizontal direction and the beam is more narrow in vertical plane. A member of the team of authors of this article had done a simulation design of 2biQUAD antenna with reflector for Wi-Fi bandwidth, but it is still in need for experimental determination of the radiation pattern to prove the theoretical model.

This article describes the experimental determination with Continuous Rotation Method (CRM) [1] of the radiation pattern of a 2biQUAD antenna with reflector for the purposes of Wi-Fi technology or other applications in different ISM frequency bands. CRM method is used to capture the radiation pattern of an antenna in determent plane. The antenna is put on a specialized stand which is rotated several times in this plane. In this way it is realized repeatedly reading the signal from the antenna, which describes the radiation pattern. With the aid of mathematical processing the received periodically repeated data is processed to minimize the random errors and improve the accuracy of the experiment.

[1]Kalina Kalinovska is a student at Faculty of Telecommunications at Technical University of Sofia, 8 Kl. Ohridski Blvd, Sofia 1000, Bulgaria. kalina.kalinovska@gmail.com

[2]Kliment Angelov, chief assistant professor, PhD is with the Faculty of Telecommunications at Technical University of Sofia, 8 Kl. Ohridski Blvd, Sofia 1000, Bulgaria. E-mail: kna@tu-sofia.bg;

II. DESCRIPTION OF THE PROBLEM

A. The 2biQUAD antenna conception

It is known different types of loop antennas with different loop shapes [2]. Some of them have a shape close to a square, which can be used in the range of HF. These antennas have uneven radiation pattern and can not satisfy the condition of omni-directional antenna for broadcasting in one plane. Combining two biQUAD antennas located in two perpendicular planes would contribute to the alignment of the omni-directional radiation pattern. On the other hand, by placing the reflector above the structure we can obtained a limited radiation pattern in vertical plane. Such an antenna can be used to realize the Wi-fi HotSpot in a conference halls or shopping centres, using a ceiling mounting. Figure. 1 shows a general view of 2biQUAD antenna with reflector.

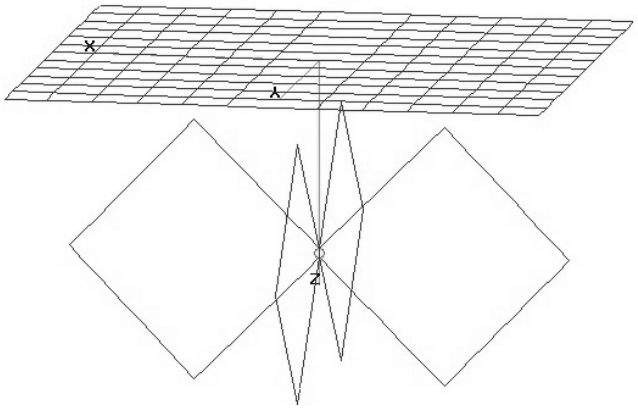

Figure 1 - 2biQUAD antenna common view

Based on the idea of two 2biQUAD antenna with reflector were made simulations of two prototypes. One is for operating frequencies matching Wi-Fi technology, and the other - intended for use in ISM band at 433 MHz. Figure 2 shows a simulation resulting radiation pattern in three-dimensional space, and Figure 3 - diagrams directional horizontal and vertical plane.

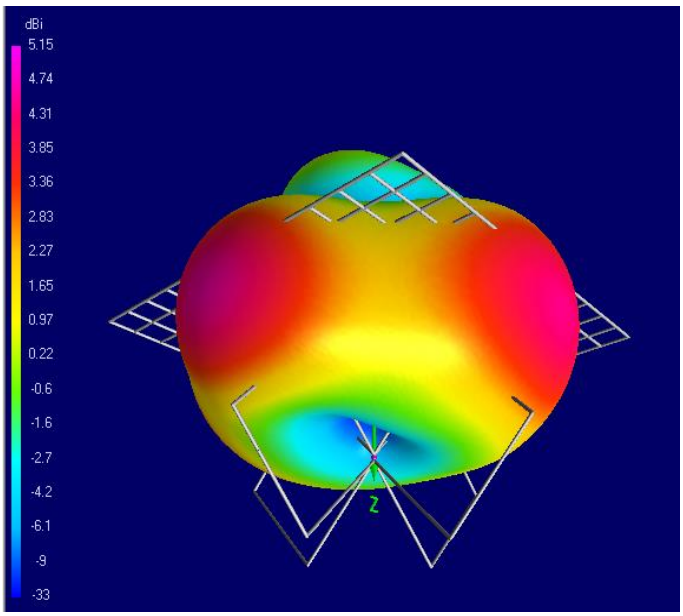

Figure 2 - 2biQUAD antenna simulated 3D radiation pattern

The defining of horizontal and vertical plane of the antenna is based on the above mentioned reasons for ceiling mounting in case of HotSpot realizations.

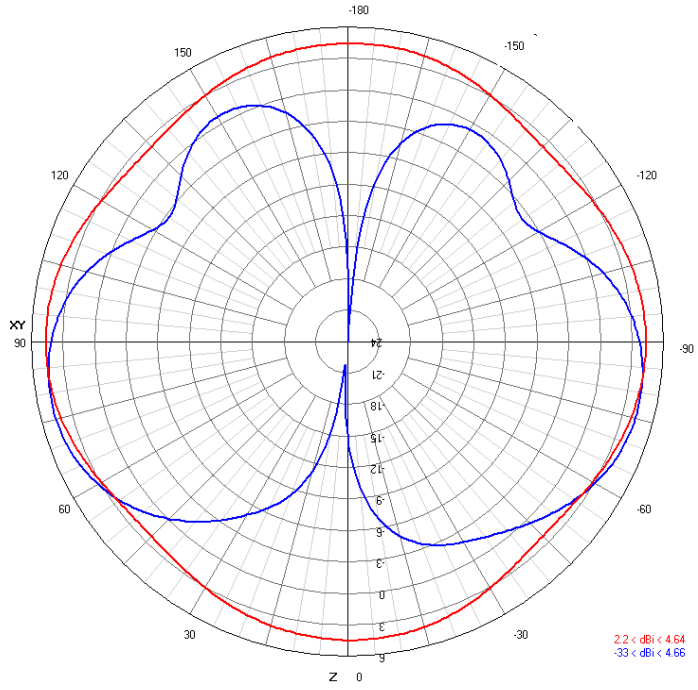

Figure 3 - 2biQUAD antenna simulated radiation pattern (horizontal and vertical)

After the simulation optimizing were relized two prototypes. One for Wi-Fi technilogy (2,45GHz) and second one for 433.05-434.79MHz frequency band. Their radiation pattern was reserched using CRM method.

B. The CRM method

Members of the team of authors of this article have developed a method for measuring diagrams of directional antennas in which is used a long multi rotation with angular velocity $\boldsymbol{\omega}$ of the test antenna (AUT). This method accumulates cyclic data with sampling time $\boldsymbol{T_s}$, through constant periodic received signal. The subsequent mathematical processing can obtain the main period of repetition and reduce random error in determining the radiation pattern. An advantage of the method is also that the current angular position is set as the relative rotation of the AUT with accuracy that can be determined by [1]:

$$\theta_{\min} = 12.T_s.\omega. \qquad (1)$$

The accuracy of the method is increasing with the number of turns of the stand. If the sampling frequency is not a multiple of the rotation frequency with angular velocity $\boldsymbol{\omega}$ then each discrete reporting occurs in different point in the radiation pattern. With this way every turn will measure unique point of the polar coordinate system set for the radiation pattern. After mathematical processing the different discrete measurements will form one radiation pattern. A similar approach is appropriate for measuring the radiation pattern of 2biQUAD antenna with reflector. Figure 4 shows the principled scheme of the experimental set. In this experiment an interest is the radiation pattern in vertical plane, since the horizontal is expected to differ minimally from omidirectional.

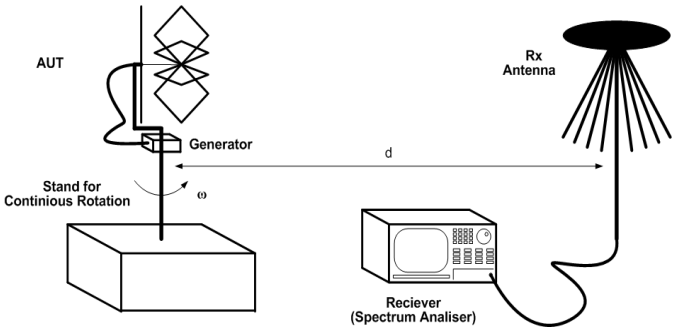

Figure 4 - Scheme of Test Stand for Radiation Pattern Measurements of 2biQUAD antenna in vertical plane

In Table 1 is given initial parameters for capturing the radioation pattern of the physical prototypes. The distance between the Tx and Rx antenna must be more than the near field of the antenna (2) [4][5]:

$$d > \frac{2.D^2}{\lambda}, \qquad (2)$$

In Figure 5 is shown a photograph of the actual implementation of the test. In it 2biQUAD antenna with reflector is placed on a stand witch provide constant rotaition.

To reduce external interference the test with prototipe on 433,92MHz was held on the roof of one of the buildings of the Technical University - Sofia.

Figure 5 – Photograph of Test Implementation

TABLE I
TEST INITIAL PARAMETERS

AUT	Type	2biQUAD
	Maximal Dimension	0,6 m
	Theoretical Directivity	5,15 dBi
Transmitter	Frequency	433,92 MHz
	RF Power	0 dBm
Measuring Distance		10 m
Rotation speed		~54 rpm
Receiving Equipment	Spectrum Analyser	GSP-830
	Receiving Antenna	Omnidirectional
	Sampling Speed	$1s^{-1}$

III. RESULTS

Using the above described method was reported CRM data. This data is describing 10 rotations of the 2biQUAD antenna with reflector. Figure 6 shows the periodic variation of the received signal for the rotations of the prototype with working frequency 433,92MHz.

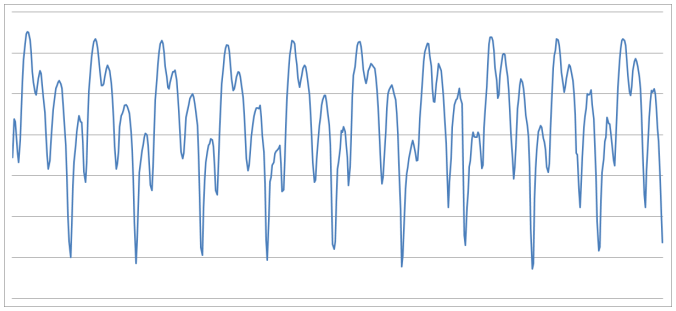

Figure 6 - Received Signal on Periods of Ten Revolutions of AUT

There was made a mathematical determination of the period of repetition of the received signal. The method is also used to reduce random errors that occurs in the experimental determinated radiation pattern. For the calculations was used the programming environment of MatLab [6]. Figure 7 shows the experimentally obtained radiation pattern in vertical plane for the prototype in 433,92 MHz frequency band.

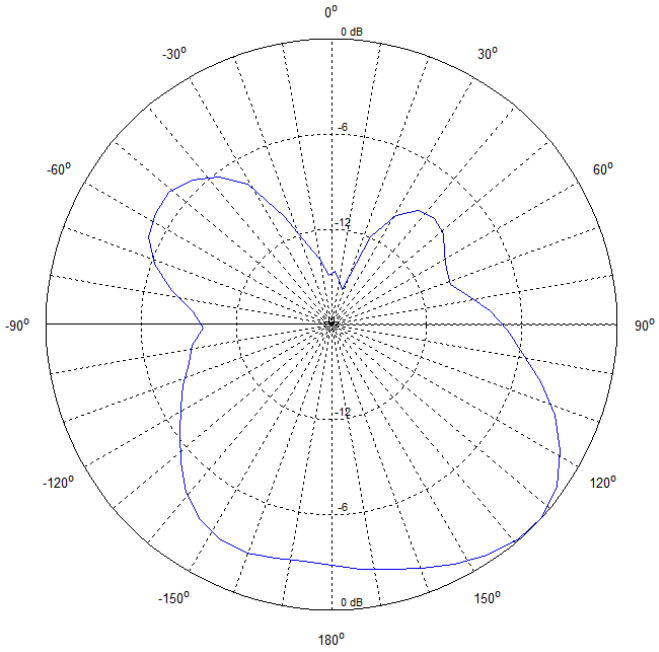

Figure 7. Experimental Radiation Pattern of AUT @ 433,92 MHz

Similarly is the experimental radiation pattern of the prototype for Wi-Fi frequency band. A graphic is shown in Figure 8. The radiation pattern varies because of the different conditions that the experiment was made. This experiment was held in a laboratory because of the weather conditions. There were many reflections from the walls and etc.

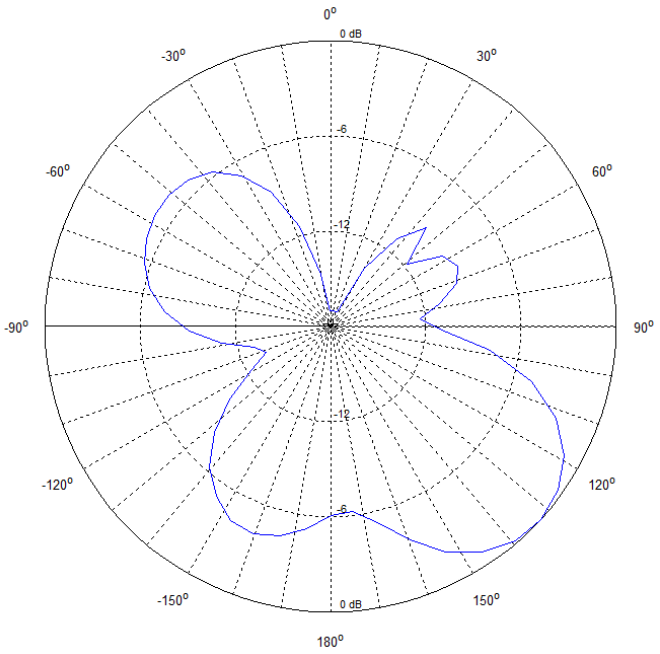

Figure 8 - Experimental Radiation Pattern of AUT @ 2,45 GHz

The obtained experimental radiation pattern of 2biQUAD antenna with reflector shows that it is suitable for the proposed use, which provides radio coverage of a HotSpots. Figure 9 shows clearly the idea of using this type of antenna to provide Wi-Fi access.

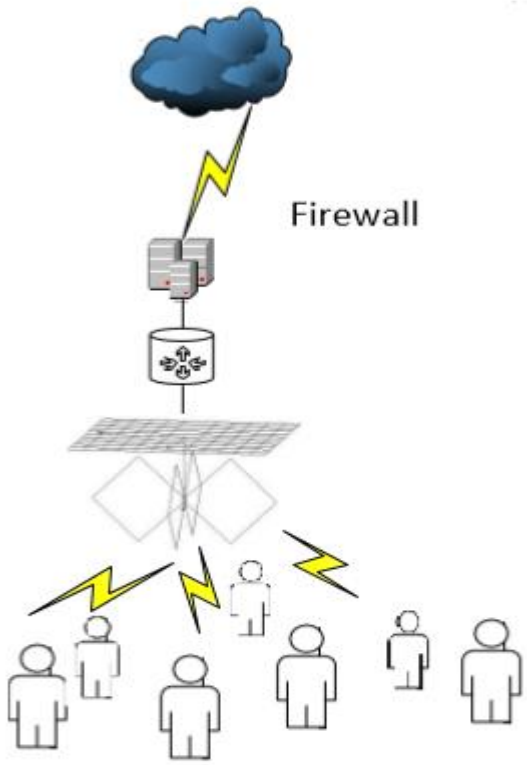

Figure 9 – An example of practicle application of 2biQUAD antenna with reflector in Wi-Fi frequency band

IV. Conclusion

Based on the experimental results the following conclusions can be made:

- 2biQUAD antenna with reflector has a omni-directional radiation pattern in horizontal plane;
- Despite some irregularities in experimental readings the results confirmed the simulations of the diagram of this type of antenna in a vertical plane,
- 2biQUAD antenna reflector is suitable in case of installing HotSpot with ceiling mounting;

Acknowledgement

In the realization of the experimental research shown in this paper, the measurement equipment was provided by TEKOMA ENGINEERING Ltd and was acquired with the support of the Operational Program „Development of the Competitiveness of the Bulgarian Economy" 2007-2013, co-financed by the European Union through the European Regional Development Fund and the state budget of Republic of Bulgaria under contract BG161PO003-1.1.05-0226-C0001.

References

[1] Gechev M., K. Angelov, B. Kehayov, S. Denev, S. Kremenski, Continuous Revolution Method for Antenna Radiation Pattern Measurements, L International Scientific Conference On Information, Communication And Energy Systems And Technologies ICEST 2015, Proceedings of Papers Vol. 1 (pp 143-146), 24 - 26 June 2015, Sofia, Bulgaria.

[2] Jonson, R. C., Antenna Engineering Handbook, 3-rd ed., McGraw Hill, 1993.

[3] Collin R. E.,Antennas and Radiowave Propagation, McGraw-Hill, 1985.

[4] Antenna Measurement Theory, Introduction to Antenna Measurement, Reprinted with the permission of ORBIT/FR Inc., www.orbitfr.com

[5] Foegelle M. D., Antenna Pattern Measurement: Concepts and Techniques, Reprinted from Compliance Engineering, Annual Reference Guide 2002 • Copyright © 2002 Canon Communications LLC

[6] MATLAB IMAGE PROCESSING TOOLBOX. User's Guide, "The Math - Works Inc.", 2000. www.mathworks.com

Infrared investigation on the thermal field in the case of influence of low frequency magnetic signals on live tissue

Kalin Dimitrov [1]

Abstract – **This paper presents a study on human skin surface warming during physiotherapy with electromagnetic field. The case is for low-frequency magnetic signal therapy with frequencies lower than 100Hz. For the experiment was used the connection between the optical radiation of the objects themselves and their temperature. The study was conducted under clinical conditions during regular physiotherapy sessions with patients. The measurements were done simultaneously at many points by using an infrared camera. The conditions in the rooms and the condition of the patients were taken into account. The emissivity coefficients of the objects studied were also considered.**

Keywords – **Infrared thermography, medical applications, magneto therapy.**

I. INTRODUCTION

With the development of technology every day we are facing new perspectives in health care – both diagnostically and therapeutically. What is observed in the last few years is an increasingly more significant implementation of infrared thermal-imaging-based medical apparatus, generally in the diagnostic sphere. However, the potential of this technology in contemporary medicine is still to be explored in further detail. The current paper is an attempt to broaden the view and deepen the understanding of some of the existing therapies (magneto therapy with low frequency magnetic field) through the analysis of data provided by a thermal camera [7-13].

Physiotherapy is a branch of medicine. Its power lies in using energy sources directed to particular areas of the body. This energy is directed in a specific way, for the prophylactics or treatment of different diseases. The sources can be natural or artificially created by people. In some cases, physiotherapy is applied as an accompanying treatment in aid of the main one. It is conducted by doctors (therapists) which define the parameters of the procedures and the course of the treatment very precisely. Physiotherapy is applied for different ages and diseases and it provides wide possibilities for influencing the human organism (electrotherapy, inductothermia, ultra-high frequencies treatment, aero-ionisation therapy, magnetic-therapy, ultra-sound therapy, lasers, magnet and laser, light-treatment, electrophoresis, diadynamic therapy, amplipulse therapy in ophthalmology, transcranial and transvertebral micropolarization, muscle toning, cryotherapy, inhalers, oxygen therapy, water treatment, warm-treatment, etc).

The effects on the human body caused by high intensity electric fields, such as muscle stimulation, electroporation and heating, are relatively well studied. We are interested in the effects caused by low intensity magnetic fields. [14-24]. The biological processes which occur are mainly related to signal transduction at the cell membrane and subsequent biochemical processes. The physical mechanisms of conversion from an electric or magnetic field to biochemical process are however subject of science studies at the present time. It is also a subject of study which aspect of the applied or environmental field is important. Properties such as duration, polarization and harmonic content of the signal, may turn out to be as important as amplitude. The effectiveness of the applied field will also be influenced by the biological, chemical and mechanical condition of the organism. A few experimentally observed results show specific biological effects which are caused directly by the magnetic field or by the electric field that is induced in the tissue by a time varying magnetic field. For fields larger than about 100 μT direct effects have been suggested and the presence of magnetite particles in some tissues may also play a biological role. Experiments suggest that effects of induced electric fields are particularly likely when their magnitudes at the tissue or cell level are relatively large and when multiple cells are connected by gap junctions. Most proteins have a small net electrostatic charge and nucleic acids are polyelectrolytes with large net charge and are surrounded by counterions. Induced fields mainly affect the moving ions on the cell surface and possibly the structural fluctuations of nucleic acid molecules. The mechanisms for direct interaction of time varying magnetic fields with biological processes are the subject of many studies.

Other experimental results have suggested that the relative magnitude and direction of a static magnetic field (such as that of the Earth) can determine the biological effectiveness of a simultaneously present alternating field in some biological systems under controlled laboratory conditions.

Very few scientific studies consider a simultaneous investigation of the effects caused by a low frequency magnetic field with infrared thermography [25-27].

II. CURRENT STATE OF THE PROBLEM

In this paper, we are going to focus on the application of magnetic-therapy. More specifically, we are going to consider the extent to which we can neglect the surface warming of the

[1]Kalin Dimitrov is with the Faculty of Telecommunications at Technical University of Sofia, 8 Kl. Ohridski Blvd, Sofia 1000, Bulgaria., kld@tu-sofia.bg

skin during the conducting of this therapy [15,17,18,20,21,23,24].

The mechanism of this type of therapy is based on a flow of electrical charges causing a net flow of ionic current for basic cellular restoration activities. Many studies show that healing effects are observed: cytoprotection of cells and the stimulation of growth factor synthesis. Contemporary devices can generate signals with a different shape, frequency and length. The frequencies used are between 1 and 100 Hz, magnetic flux density being up to 100 mT. There are 3 established physical mechanisms through which pulsed magnetic fields interact with living matter: magnetic induction, magnetomechanical effects and electronic interactions, which is thought to be responsible for the vasodilatation, analgesie, anti-inflammatory, anti-edematous and spasmolytic activity and healing acceleration. There is an overall improvement of the microcirculatory processes and local blood circulation.

Depending on the cases (diseases, people), suitable inductors are used.

Usually the period of the therapy includes 20 procedures every day or every other day. In the case of special medical recommendation it is possible to do two procedures per day (in the morning and in the afternoon).

The magneto therapy is well combined with other physical factors (laser therapy, interfered currents, ultrasound therapy, water and mud treatments). The magnetic field can be well combined with drug treatment, too.

III. Experiments

The thermal camera used for data collection was FLIR E40, with thermal sensitivity of < 0.07°C and temperature range of (-20°C to 650°C) [28]. For maximum accuracy, the camera was fixed on a stand and movement of the object was avoided. All examinations were performed in a sitting position in a quiet room at a constant room temperature of 20±0.5°C following an acclimatization period of 20 min keeping the hands free of any contact to the rest of the body or other objects [29]. Equally, the relative humidity showed stable values over time (50%). All temperature maps were archived using the internal SD memory. For the final analysis temperature values were determined and given in degrees Celsius (°C). All images were corrected using an emissivity factor of 0.98 for the human skin and appropriate emissivity factors for the fabric and plastic, respectively 0.77 and 0.91. For the human hair emissivity factor we assume the value of 0.98.

In this study, a series of images was made between certain intervals of time. The infrared pictures were taken at intervals of 30 sec. for 15 minutes. The therapy duration was determined by the doctor in charge. The infrared pictures do not influence the main therapy, so there are no special requirements on the part of doctors apart from the general requirements for hospital hygiene and rules.

The processing was made with the original software of the camera - version FLIR Tools+ 5.3.1 (5.3.15320.1002).The setting is shown in fig.1.

During the experiment were taken 30 pictures. The first one is shown in fig. 2.

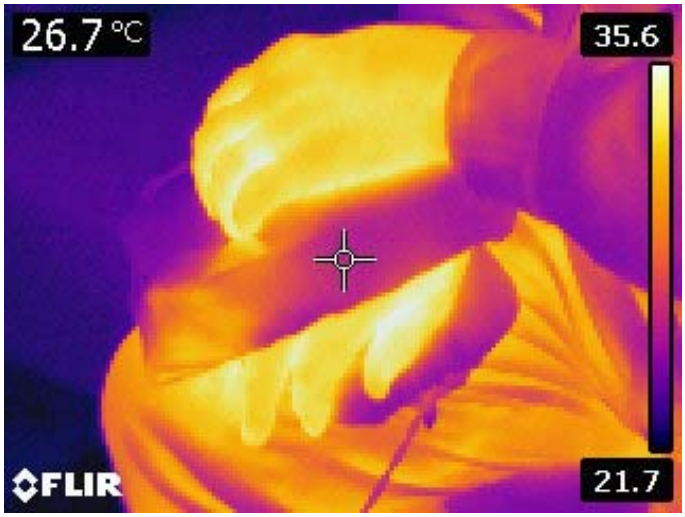

Fig. 1. Therapeutic procedure

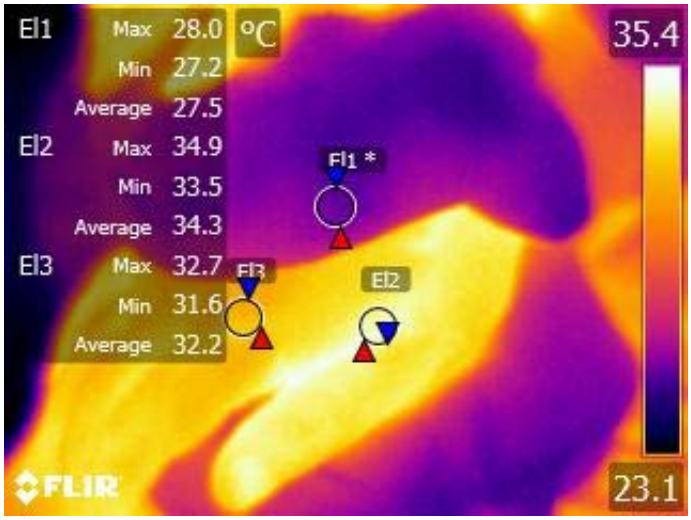

Fig. 2. An image from the magneto therapy series

Three ellipses of interest were selected: El1 – on the textile wrapping of the magnet; El2 – in the area of the most intense thermal radiation of the hand; El3 – in the area closest to the metacarpophalangeal joint. We selected ellipses, not points, to eliminate probable human movements and noises. For the areas where the human skin is observed, is selected a radiation coefficient 0.98 and for the fabric-wrapped magnet is selected a radiation coefficient 0.77 [12].

IV. Results

The first calculations, of course, are related to the mathematical expectation, dispersion and standard deviation. By using the respective formulae [30,31], we derive (Table I):

A. MAGNETO THERAPY

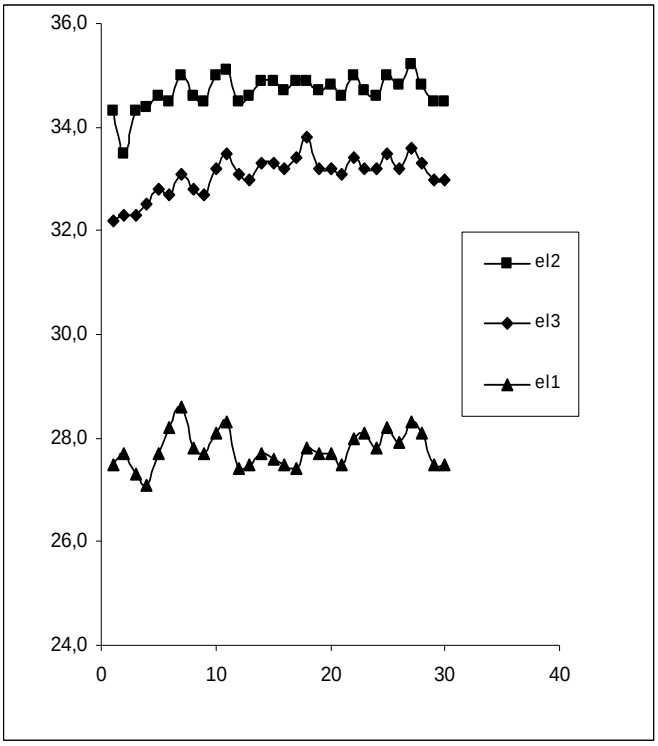

Fig. 3. Graphic representation of measurements during the experiment with magneto therapy (x-axis – number of experiment; y-axis – temperature)

TABLE I. CALCULATION OF THE AVERAGE VALUES, DISPERSIONS AND STANDARD DEVIATIONS

	El1	**El2**	**El3**
AVG	27,773333	34,68	33,07
VAR	0,1192644	0,105103	0,151138
sqrt(VAR)	0,3453467	0,324197	0,388765

V. CONCLUSION

The analyzed data gives one more perspective of the countless applications of thermal imaging cameras for medical purposes. Such analysis can be very useful in providing a new understanding of widely used technology in terms of safety and effectiveness in physiotherapy. Since IR imaging is non-invasive and does not bear any risks, it can be implemented wherever it is useful and possible. It also carries a great potential for diagnostic medicine to search for different connections between the points of the temperature filed and completely different phenomena.

ACKNOWLEDGEMENT

This research was supported by the personnel of Studentska Polyclinic and Technical University of Sofia. We would like to thank them for facilitating this research and providing the appliances to analyze.

We would also like to thank Prof. Dimitar Dimitrov for assisting whenever needed and for providing comments that greatly improved this paper.

REFERENCES

[1] P. Childs, (et. all), *Practical Temperature Measurement. Butterworth Heinemann*, Elsevier, 2001.

[2] I. Fernández-Cuevas, J. C. Bouzas Marins, J. A. Lastras, P. M. G. Carmona, S. P. Cano, M. Á. García-Concepción, M. Sillero-Quintana, "Classification of factors influencing the use of infrared thermography in humans: A review", *Elsevier, Infrared Physics & Technology*, Elsevier, 71, pp.28–55, 2015.

[3] R. Fuksis, M. Greitans, O. Nikisins, M. Pudzs, "Infrared Imaging System for Analysis of Blood Vessel Structure", Electronics and Electrical Engineering, No.1(97), pp.45-48, 2010.

[4] A. Szentkuti, H. S. Kavanagh, S. Grazio, "Infrared thermography and image analysis for biomedical use", Periodicum Biologorum, Vol. 113, No. 4, pp.385–392, 2011.

[5] S. Pleshkova, A. Bekyarski, K. Peeva, "Testing Thermal Images Characteristics for Thermal Images Quality Estimation", Latest Trends on Systems, 18th International Conference on Systems, Vol.1, pp.251-256, 2014.

[6] S. Pleshkova, A. Bekyarski, "Motion Detection in Thermal Images Sequence Using Wigner Distributions", Latest Trends on Systems, 18th International Conference on Systems, Vol.1, pp.153-156, 2014.

[7] J. Serup, G. B. E. Jemec, G. L. Grove, Handbook of Non-Invasive Methods and the Skin, Second Edition, CRC Press, 2006.

[8] B. Jones, "A reappraisal of the use of infrared thermal image analysis in medicine", 17(6), IEEE Trans Med Imaging, pp.1019-27, 1998.

[9] F. Ring, A. Jung, J. Żuber, *Infrared Imaging*, IOP, 2015.

[10] S. Nudelman, *Nuclear Medicine, Ultrasonics, and Thermography*, Springer Science & Business Media, 2013.

[11] M. Diakides, J.D. Bronzino, D. R. Peterson, Medical *Infrared Imaging: Principles and Practices*, CRC Press, 2012.

[12] Y. Houdas, E.F.J. Ring, Human Body Temperature: Its Measurement and Regulation, Springer Science & Business Media, 2013.

[13] E. Salazar-López, E. Domínguez, V. Juárez Ramos, J. de la Fuente, A. Meins, O. Iborra, G. Gálvez, M.A. Rodríguez-Artacho, E. Gómez-Milán, "The mental and subjective skin: Emotion, empathy, feelings and thermography", *Elsevier, Consciousness and Cognition*, 34, pp.149–162, 2015.

[14] Ueno S., *Biological Effects of Magnetic and Electromagnetic Fields*, Springer Science & Business Media, 2007.

[15] Petreus D., Patarau T., Etz R., Kiraly E., Baru P.E., Low frequency pulsed magneto therapy microsystem, Electronics Technology (ISSE), 36th International Spring Seminar on, pp.372 – 377, 2013.

[16] M. S. Markov, *Electromagnetic Fields in Biology and Medicine*, CRC Press, 2015.

[17] D. Dimitrov, A. Dimitrov, "Visualisation of Space-Temporal Configuration of Low Frequency Magnetic Signals", Electronics and Electrical Engineering, No.3(109), pp.46-48, 2011.

[18] D. Dimitrov, "Visualization of a Low Frequency Magnetic Field, generated by Girdle Coil in Magnetotherapy", Electronics and Electrical Engineering, No.6(78), pp.57-60, 2007.

[19] A. Presman, *Electromagnetic Fields and Life*, Springer Science & Business Media, 2013.

[20] A. del Morala, María J. Azanzab, A model explaining synchronization of neuron bioelectric frequency under weak alternating low frequency magnetic field Journal of Magnetism and Magnetic Materials, Vol.377, pp.298–307, Elsevier, 2015.

[21] J. Wilson, J. Haines, Z. Sienkiewicz, Y. Dubrova, The effects of extremely low frequency magnetic fields on mutation induction

in mice, Mutation Research/Fundamental and Molecular Mechanisms of Mutagenesis, Vol.773, pp.22–26, Elsevier, 2015.

[22] C. Polk, Biological Effects of Magnetic and Electromagnetic Fields, (chapter) pp. 63-83, Biological Effects of Magnetic and Electromagnetic Fields, Springer, 1996.

[23] C.L.M. Bauréus Koch, M. Sommarin, B.R.R. Persson, L.G. Salford, J.L. Eberhardt, Interaction between weak low frequency magnetic fields and cell membranes, Bioelectromagnetics, Vol. 24, Issue 6, pp.395–402, Wiley-Liss, Inc., 2003.

[24] F. Prato, M. Kavaliers, A.W. Thomas, Extremely low frequency magnetic fields can either increase or decrease analgaesia in the land snail depending on field and light conditions, Bioelectromagnetics, Vol. 21, Issue 4, pp. 287–301, Wiley-Liss Inc. 2000.

[25] E. Boerner, J. Bauer, B. Ratajczak, E. Deren, H. Podbielska, "Application of thermovision for analysis of superficial temperature distribution changes after physiotherapy", Springer, J Therm Anal Calorim, 120, pp.261–267, 2015.

[26] A. Domingues, E. M. Pereira, J. Gabriel, R. Vardasca, "Case Study in Thermal Monitoring of Physiotherapy Treatments to Ankle Sprains in Rugby Athletes", Pan American Journal of Medical Thermology, vol.1, No.1, pp.3-10, 2014.

[27] A. Seixas, S. Rodrigues, V. Soares, T. Dias, R. Vardasca, J. Gabriel, "Thermographic assessment of a physiotherapy related upper limb task: Preliminary study", Occupational Safety and Hygiene III, pp.273-277, 2015.

[28] http://www.flir.com/cs/emea/en/view/?id=41372 - FLIR Systems, Inc.

[29] K. Ammer, "The Glamorgan Protocol for recording and evaluation of thermal images of the human body", Thermology International, 10, 18(4), 2008, pp.125-129.

[30] Morten Brons, Martin Philip Bendsoe, Mads Peter Sorensen, Progress in Industrial Mathematics at ECMI 96, Springer-Verlag, 2013.

[31] H.C. Taneja, Advanced Engineering Mathematics, I. K. International Pvt Ltd, 2007.

Statistical Characteristics of Optimal Divergence of Laser Beam at FSO Systems

Tsvetan Mitsev[1]

Abstract – **In this paper a methodology for calculating the statistical characteristics of the optimal divergence of the laser beam at free space optics systems is developed. It estimates the probability density function of meteorological visibility through the use of statistical material on the likelihood of different weather conditions. The statistical characteristics of the optimal divergence of the laser beam using a deterministic relationship between it and the meteorological visibility are calculated. A simplified model for calculating the volume coefficient of the atmospheric extinction is proposed. Its spectral dependence is taken into account**

Keywords **– FSO, optical wireless communication systems, probability density function, laser beam optimum divergence.**

I. INTRODUCTION

The main problem with the reliability of the work of free spase optics (FSO) systems occurs in the presence of fog and haze. In a dense fog meteorological distance of visibility V [km] may be reduced and reach values of a few tens of meters to several meters. Relative to attenuation b (respectively to volume extinction coefficient α [1/km]) in the communication channel, this corresponds to the values of the order of hundreds of dB/km.

In most works related to the model description of the communication channel, it is assumed homogeneous channel, i.e. constant attenuation along the length of the communication channel. This is due mainly to convenient for use in theoretical analyzes semi-empirical relationship between attenuation and meteorological visibility (the meteorological visibility reflects integrally the status of the communication channel, along it's entire length) [1], [2]. In modeling the communication channel attenuation b is determined mostly by empirical data on meteorological visibility [3], [4]. Most works devote attention to the wavelength of the optical radiation λ, i.e. to the spectral attenuation depending on the weather conditions [5], [6]. There are also models for prediction and analysis of the effects of fog on the operation of FSO communications system. [7], [8], [9].

In recent years, much attention is paid to the stochastic nature of fading of optical radiation into fog and to the study of statistical characteristics of the atmospheric channel. In contrast to the statistical characteristics of the communication channel of radio frequency wireless communication systems, which long ago are well studied, only recently more attention is paid to the study of statistical characteristics of communication channel of FSO systems [10]. Taking into account the stochastic nature of attenuation of optical radiation in the atmospheric channel of communication is the main factor that contributes to increasing the reliability of operation of these systems. Of particular importance is the modeling of optical communication channel in terms of fog and smoke or haze. This involves a lot of experimental work and theoretical research. An important step towards overcoming the impact of weather conditions and increasing opportunities for data transmission with FSO systems is statistical modeling of atmospheric communication channel.

In our previous work we consider the possibility of increasing the quality indicators of FSO systems through correct choice of divergence of optical radiation θ_t [rad] of the transmitter during process of instalation [11], [12]. Also it is possible automatic adjustment of the divergence of optical radiation of the system during the working process. In [13] formula for calculating the optimum value of divergence angle $\theta_{t,opt}$ depending on various parameters of the system and of the atmospheric communication channel is derived. Studies were made on the assumption of uniform and stationary atmospheric communication channel.

In this work we start building of statistical description of the communication channel of the FSO system. We use statistical data on the histogram of meteorological distance of visibility. The data used are for years. They refer to the northern hemisphere. A model of probability density function (PDF) of meteorological distance of visibility is built. The resulting PDF is used to calculate the statistical characteristics of meteorological visibility. A deterministic relationship between the optimal divergence of optical radiation of the transmitter $\theta_{t,opt}$ of FSO system and meteorological distance of visibility is presented. Through this connection expressions to calculate the statistical characteristics of $\theta_{t,opt}$ are derived and are calculated for a particular case.

II. THEORY

As we noted in the introduction, in recent years more and more attention is paid to the statistical nature of the work of FSO systems. This is in direct relation to the increase of their reliability of work.

In our works [14] and [15] we showed that serious importance to increasing the time during which the system will operate with values of *BER* under specified maximum value is setting the divergence of optical radiation of the transmitter of its optimal value $\theta_{t,opt}$ [rad]. Its value depends on the value of the random variable meteorological visibility distance V [km]. Therefore $\theta_{t,opt}$ also is a random variable. To determine its statistical characteristics we need to know those on V.

[1]Tsvetan Mitsev is with the Faculty of Telecommunications at Technical University of Sofia, 8 Kl. Ohridski Blvd, Sofia 1000, Bulgaria, E-mail: mitzev@tu-sofia.bg.

In the literature is published for a given area and for a chosen season (or time period, usually annual) average statistical data on the percentage of the total time during which there is a particular weather conditions. Because surroundings are varied, mists, fogs, rain or snow, general characteristics, which can be summarized is meteorologival visibility *V*. In fact, this is the characteristic important for the work of the FSO system. It is associated with volume extinction coefficient α [km^{-1}], and through it to the transparency of the communication channel τ_a. The last characteristic is fundamental to energy balance (the change of power from the transmitter to the receiver) of the FSO systems.

A. Visibility probability density function (PDF)

Usually we have a histogram of the distribution of meteorological distance of visibility *V*. These are presented in tabular form statistical data on average time as a percentage of total in the year *p* [%] in which there is a particular weather conditions. Any weather conditions are characterized by an appropriate range of values of meteorological distance of vision (visibility) ΔV_i [km] = $V_{i+1} - V_i$, $i = 1, 2, 3 \ldots$.

Based on these data can be calculated statistical characteristics of meteorological visibility *V*, viewed as a random variable: probability density function (PDF) *f*(*V*) [km^{-1}], mathematical expectation m_V [km], dispersion σ_V^2 [km^2], average square deviation σ_V [km]. To make a step shaped line *p*(*V*) at a probability density function *f*(*V*) we must comply with the condition [16]

$$\int_{-\infty}^{\infty} f(V).dV = 1. \qquad (1)$$

In the case of a stepped (step shaped) function with finite range (limited by physical considerations above and below) the condition (1) is converted to

$$\sum_i f_i \Delta V_i = 1, \quad f_i = f(V \in [V_i, V_{i+1}]) = \text{const}. \qquad (2)$$

The last equality and the condition

$$\sum_i K.p_i \Delta V_i = 1$$

give us the relationship

$$f_i = K.p_i, \quad K = \frac{1}{\sum_i p_i.\Delta V_i}. \qquad (3)$$

By determining the probability density function *fi* we easily determine other statistical characteristics of *V* [15],

$$m_V = \int_{-\infty}^{\infty} V.f(V)dV \qquad (4)$$

and

$$\sigma_V^2 = \int_{-\infty}^{\infty} [V - m_V]^2.f(V)dV = \int_{-\infty}^{\infty} V^2.f(V)dV - m_V^2. \qquad (5)$$

Of course for the practical calculations of m_V and σ_V^2 we also replace integrals in (4) and (5) with sums like in (1).

B. Relationship between volume extinction coefficient and meteorological distance of vision (visibility

Deterministic relationship between $\theta_{t,opt}$ and *V* is implemented through transparency of the communication channel τ_a and volume extinction coefficient α. In the literature, the most commonly used semi-empirical relationship is

$$\alpha\left[\text{km}^{-1}\right] = \frac{3,92}{V[\text{km}]}\left(\frac{\lambda[\mu\text{m}]}{0,55}\right)^{-0,585\sqrt[3]{V[\text{km}]}}. \qquad (6)$$

This relationship is characterized by: it has relatively inconvenient form for theoretical analysis; it applies to the $V \leq$ 10 km. Therefore, the work offer more convenient for mathematical calculations relationship

$$\alpha = A.V^{-Q}, \qquad (7)$$

where the coefficients *A* and *Q* are spectrally dependent. In Tablet I are attached values of *A* and *Q* for three values of the wavelength of the optical radiation λ. The last column is a maximum relative error between the values of α calculated by formulas (7) and (6). Calculations were made for a range of values of meteorological distance of visibility *V* [km] $\in$ [0,02; 100].

TABLE I
VALUES OF SPECTTRAL COEFFICIENTS *A И Q*

λ [μm]	*A*	*Q*	$\Delta\alpha_{max}$ [%]
0,85	2,87	1,08	7,28
1,31	2,11	1,16	15,53
1,55	1,87	1,2	22,97

C. Calculation of the statistical characteristics of $\theta_{t,opt}$ by numerical integration

In our work [11] is taken out the deterministic relationship between random quantity $\theta_{t,opt}$ and random quantity *V*, namely

$$\theta_{t,opt} \equiv \theta = \frac{1}{z}\sqrt{\frac{2.\tau_t.\Phi_L}{\pi.e.I_{min}}}\sqrt{e^{-\alpha(V).z}}, \qquad (8)$$

where *z* [km] is the length of the communication channel; τ_t is the transmission of transmitter optical antenna; Φ_L [W] is the power of the laser pulses (i.e. bit entity in IM / DD and

OOK modulation); e is the base of natural logarithm; I_{min} [W/m^2] is the minimum intensity of the optical radiation into the aperture of the photodetector.

The minimum intensity I_{min} depends on many parameters of the receiver and different physical constants. It is selected so that satisfies the information capacity of the systems C_I [bps] and and the specified maximum value for bit error BER_{max}, which will operate the system.

If it is known a PDF of V and using equation (3) and connection (8), we can determine the statistical characteristics of θ [16]

$$m_\theta = \int_{-\infty}^{\infty} \theta(V).f(V).dV\,, \tag{9}$$

$$\sigma_\theta^2 = \int_{-\infty}^{\infty} [\theta(V) - m_\theta]^2 . f(V).dV = \int_{-\infty}^{\infty} \theta^2(V).f(V).dV - m_\theta^2\,. \tag{10}$$

Of course, here, similarly to (1), due to the step shaped dependence $f(V)$, replacing the solution of the integrals with the sums. In this case the inner integrals for the different members of the sum, i.e., within the ranges ΔV_i, we solve numerically.

III. Results and Discussions

To test developed methodology for calculating the statistical characteristics of optimum divergence of the laser beam at FSO systems we will use enclosed in [17] tabulated statistical average data on the percentage of time during the year in which there is a different weather conditions. The data refer to the northern hemisphere of the Earth (Tab. II, columns 2 and 4). The values of meteorological distance of visibility V are divided into 11 spaces. The probability of a fall of V into the final two spaces is zero. On the basis of these data has been obtained the probability density function of V in column 6.

TABLE II
PROBABILITY DENSITY FUNCTION OF METEOROLOGICAL DISTANCE OF VISIBILITY V

i	V [km]	ΔV [km]	P [%]	ΔV .P	$f(V)$ [1/km]	ΔV. $f(V)$
1	2	3	4	5	6	7
1	< 0,05	0,05	0	0	0	0
2	0,05÷0,2	0,15	0,4	0,06	3,0256E-4	4,538E-5
3	0,2÷0,5	0,3	0,6	0,18	4,538E-4	1,362E-4
4	0,5÷1	0,5	1,6	0,8	1,21E-3	6,051E-4
5	1÷2	1	4,2	4,2	3,177E-3	3,177E-3
6	2÷5	3	0,6	1,8	4,538E-4	1,362E-3
7	5÷10	5	43,4	217	3,282E-2	1,641E-1
8	10÷20	10	19,8	198	1,498E-2	1,498E-1
9	20÷50	30	28,5	855	2,156E-2	6,467E-1
10	50÷100	50	0,9	45	6,808E-4	3,404E-2
11	> 100	∞	0	0	0	0
Σ	–	–	100	1322,04	–	1

On the Fig. 1 is shown $f(V)$, as step-like character of the f(V) is replaced with a line. The line connects neighboring values *fi*. The values *fi* are built for the midpoint of each interval ΔV_i.

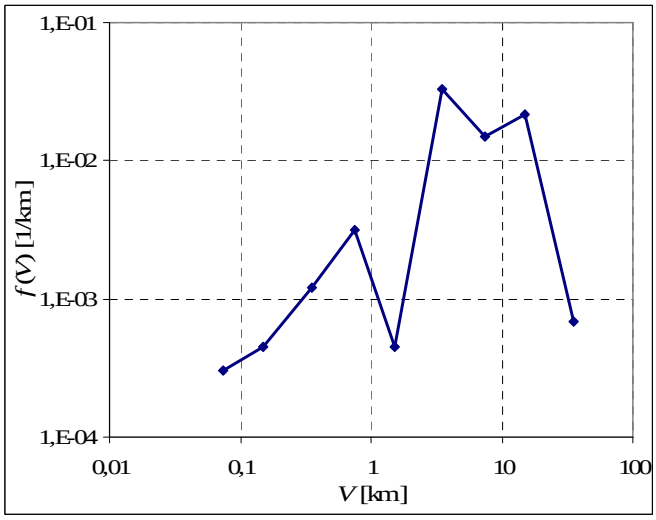

Fig. 1. Probability density function $f(V)$ of meteorological distance of visibility V

Fig. 2 shows used in the work dependencies $\alpha(V)$ calculated for the three lengths of λ. Calculation based on the expression (7) and corresponding coefficients from the Table I.

It is seen a big difference in the values of the volume extinction coefficient α for various wavelengths with increasing the value of meteorological distance of visibility V.

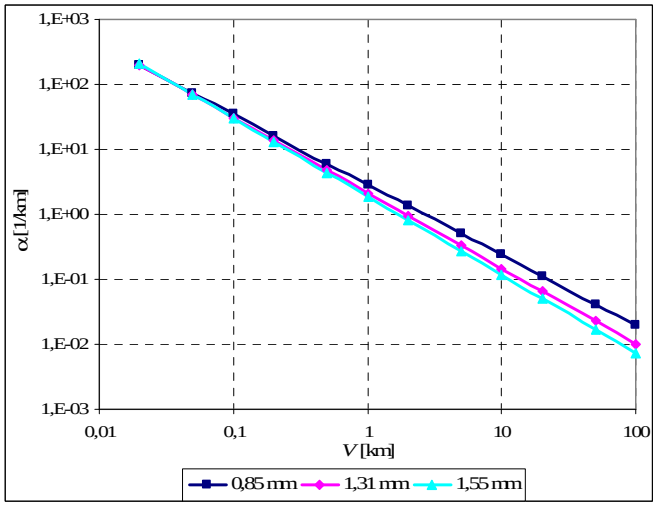

Fig. 2. Dependence on the volume extinction coefficient α of meteorological distance of visibility V

For the calculation of the statistical characteristics through (8) and (9) we choose typical values of variables involved: $z = 1$ km; $\lambda = 1{,}55$ μm; $\tau_t = 0{,}85$; $\Phi_L = 20$ [mW]; $I_{min} = 1{,}023.10^{-4}$ W/m^2. The value of I_{min} is calculated for the

average statistical parameters of the receiver. In the calculation is selected $C_l = 100$ Mbps and $BER_{max} = 10^{-8}$. In the value of I_{min} the presence of background optical radiation is reported. Calculated by the method above described values of statistical characteristics of V and of $\theta_{t,opt}$ are mapped in Table III.

TABLE III
VALUES OF STATISTICAL CHARACTERISTICS OF VISIBILITY AND OF OPTIMAL DIVERGENCE OF OPTICAL RADIATION OF TRANSMITTER

	m	σ^2	σ
V	28,7 km	261,5 km^2	16,2 km
$\theta_{t,opt}$	6,046 mrad	36,62 mrad^2	6,052 mrad

IV. CONCLUSION

Over the past decade has increased the number of scientific publications devoted to the possibilities of predicting and improving the reliability of operation of FSO systems. The reliability of the work is directly dependent on the parameters of the atmospheric channel of communication and the choice of the main parameters of the systems. The random character of the the parameters of the communication channel leads to random character of the basic parameters of the system. One of the main parameters is the optimal divergence of optical radiation of the transmitter.

The first step to a statistical analysis of reliability of FSO systems is to build real statistical model of atmospheric channel of communication, finding its statistical characteristics and related statistical characteristics of optimal divergence of optical radiation of the transmitter.

The work shows that in typical for northern hemisphere weather conditions in a communication channel with a length of 1 km and average statistical parameters of the system, the average optimal divergence is 6,05 mrad with dispersion 36,62 mrad^2.

REFERENCES

[1] Oliver Bouchet, Herve Sizum, Christian Boisrobert, Frederique de Foruel, *Free-Space Optics: Propagation and Communications*, John Wiley&Sons, 2010.

[2] Roberto Ramirez-Iniguez, Sevia M. Idrus, Ziran Sun, *Optical Wireless Communications - IR for Wireless Connectivity*, CRC Press, An Auerbach book, 2008.

[3] F. Nadeem, T. Javornik, E. Leitgeb, V. Kvicera, and G. Kandus, "Continental fog attenuation empirical relationship from measured visibility data", Radioengineering, vol. 19, p. 596-600, Dec. 2010.

[4] Heinz A. Willebrand, Baksheesh S. Ghuman, *Free-Space Optics: Enabling Optical Connectivity in Today's Networks*, Indianapolis, Sams Publishing, 2002.

[5] I. Kim, B. McArthur, E. Korevaar, "Comparison of l aser beam propagation at 785 nm and 1550 nm in fog and haze for optical wireless communications," Proc. of SPIE, vol. 4214, pp. 26-37, 2001.

[6] K. Fischer, M. Witiw, and E. Eisenberg, "Optical attenuation in fog at a wavelength of 1.55 micrometers", Atmospheric Research, vol. 87, pp. 252-258, March 2008.

[7] J. Gebhart, M. Leitgeb, E. Bregenzer, "Atmospheric effects on optical wireless links", in 7-th International Conference on Telecommunication, vol.2, pp. 395-401, Zagreb, 2003.

[8] M. Al Naboulsi, H. Sizun, F. de Fornel, "Fog attenuation prediction for optical and infrared waves", Journal of SPIE, Optical Engineering, vol 43, pp. 319-329, 2004.

[9] M. Ijaz, Z. Ghassemlooy, J. Pesek, O. Fiser, H. Le Minh, and E. Bentley, "Modeling of fog and smoke attenuation in free space optical communications link under controlled laboratory conditions", *IEEE Journal of Lightwave Technology*, vol. 31, pp. 1720-1726, April 2013.

[10] M. Khan, M. Awan, E. Leitgeb, F. Nadeem, and I. Hussain, "Selecting a distribution function for optical attenuation in dense continental fog conditions", International Conference on Emerging Technologies, pp. 142-147, Oct. 2009.

[11] Tsvetan Mitsev, Kalin Dimitrov, Hristo Ivanov, Nikolai Kolev, Optimum divergence of laser radiation in FSO systems, 7-th International Conference on Communications, Electromagnetics and medical Applications (CEMA'12), pp. 42-45, Athens, Greece, 2012.

[12] Mitsev Ts., N. Kolev, Hr. Ivanov, K. Dimitrov, Optimum Divergence of the Transmitter Optical Radiation in FSO Systems, XLVII Intern. Scientific Conf. on Inform., Communication and Energy Systems and Technol. (ICEST 2012), pp. 55-58, Veliko Tarnovo, Bulgaria, 2012.

[13] Yordan Kovachev, Tsvetan Mitsev, FSO Availability Depending on the Meteorological Conditions, 9-th International Conference on Communications, Electromagnetics and Medical Applications (CEMA'14), pp. 19-23, Sofia, 2014.

[14] Tsvetan Mitsev, Nikolay Kolev, Optimal Divergence of Laser Beam in Optical Wireless Communication Systems, Elektrotechnica & Elektronica, Vol. 49, No 11-12, pp. 15-20, 2014.

[15] Tsvetan Mitsev, Yordan Kovachev, Availability of MFSO Using Optimal System Parameters, Proceedings of 14th Conference on Microwave Techniques "COMITE 2015", April 22-23, Pardubice, Czech Republic, pp. 131-134, ISBN 978-1-4799-8121-2, 2015.

[16] E. Ferdinandov, B. Pachedjieva, Probabilistic and statistical methods in communications – Part I, Sofia, Siela, 2005. (in bulgarian)

[17] E. Ferdinandov, Laser radiation in Radio-technics, Sofia, Technics, 1981. (in bulgarian)

ANN Approach for Return Loss Analysis of Ohmic Series RF MEMS Switches

Tomislav Ćirić[1], Zlatica Marinković[1], Marija Milijić[1], Olivera Pronić-Rančić[1], Vera Marković[1], Larissa Vietzorreck[2]

Abstract – **RF MEMS switch applications in communication systems have been increased in the recent time, creating a need for reliable and accurate switch models. The model exploited for the analysis presented in this paper is based on the artificial neural networks. In particular, a model relating the lateral dimensions of the switch bridge and the switch S-parameters is considered. The model allows fast and efficient analysis of S-parameters behavior, requiring significantly shorter time for the same analyses than standard electromagnetic simulators. The main purpose of the paper is analysis of the switch return loss changes with small the changes of the bridge dimensions. The most illustrative results of the analysis are discussed and corresponding recommendations for the switch optimization are given.**

Keywords –**Artificial neural networks, Return Loss, Insertion Loss, RF MEMS switch.**

I. INTRODUCTION

RF MEMS switches are surface-micromachined devices which use mechanical movements to achieve a short circuit or an open circuit in the RF transmission-line [1]. These devices are extremely small and light and are applicable in many communication devices and systems. Also, they are highly linear and can operate up to higher frequency bands providing high isolation and low insertion loss in general. The dimensions of RF MEMS switch components have to be optimized carefully in order to fulfill the desired RF specifications. Generally, the optimization is performed by full-wave EM simulations [2]. However, simulations in standard simulators are time consuming and require considerable computing resources because the switch generally consists of several thin layers and vias with high complexity. Moreover, since the optimization process mostly involves a series of EM simulations with varying parameters, the computing load is further increased. The common method to improve simulation speed and efficiency is to use a lumped element circuit model in a circuit simulator. However, to derive an accurate circuit model is demanding, especially at high frequencies, because the circuit model should involve more parasitic components at higher frequencies, which increases the model complexity [3]. A solution to these needs can be the application of artificial neural networks (ANNs) for deriving proper models for different switch types and to relate different sets of input parameters to the desired output quantities. ANNs have been widely used as a fast and efficient tool for modeling of different electronic devices [4]-[5], among them RF MEMS devices [6]-[7]. Use of ANN based models has a great advantage in reducing the computational cost, especially when implemented within a circuit simulator that has integrated tuning and optimization options. Namely, ANNs are capable of modeling nonlinear mappings of multiple input/output parameters, providing models which enable an accurate device characterization and efficient prediction of unknown input-output relationships with low computational overhead.

ANN based modeling and optimization of an ohmic series RF MEMS switch is presented in [8]. On the base of several full-wave numerical simulations of the switch, ANNs are developed to directly relate the switch geometrical parameters to the scattering parameters over frequency. Besides the lateral dimensions of the bridge, the lateral dimensions of the gap surrounding the bridge are concerned as well. The gap size has to be adjusted in order to achieve a proper matching of the bridge section with input/output line impedance. It is reported that with the developed model an optimization of the structure can be done within seconds.

In the design of an RF MEMS switch one of the requirements to be met in the optimization is to keep return loss below a specified value in the frequency range of interest. In this paper the model presented in [8] is exploited for analysis of the switch return loss. In particular, special attention is put on analysis how the return loss deviates from the nominal values if the dimensions of the bridge membrane are changed due to their small changes caused by the fabrication tolerances. In addition, the corresponding insertion loss changes are reported in the paper.

The paper is organized as follows: After the introduction, in Section II the considered RF MEMS switch is described. The ANN model used in this work is presented in Section III. The results of the analysis of the switch return and insertion losses and the corresponding discussion are given in Section IV. Finally, Section V contains the concluding remarks.

II. MODELED DEVICE

The device considered in this work is a CPW (coplanar waveguide) based RF MEMS ohmic series switch, depicted in

[1] T. Ćirić, Z. Marinković, M. Milijić O. Pronić-Rančić, and V. Marković are with the University of Niš, Faculty of Electronic Engineering, Aleksandra Medvedeva 14, 18000 Niš, Serbia
E-mail: cirict78@gmail.com, zlatica.marinkovic@elfak.ni.ac.rs, marija.milijic@elfak.ni.ac.rs, olivera.pronic@elfak.ni.ac.rs, vera.markovic@elfak.ni.ac.rs

[2] L. Vietzorreck is with the TU München, - Lehrstuhl für Hochfrequenztechnik, Arcisstr. 21, 80333 München, Germany, e-mail: vietzorreck@tum.de.

Fig. 1a. The switch is fabricated at FBK in Trento on a 525µm thick silicon wafer by standard surface micromachining and CMOS technologies, which requires eight masks, [9]. A serious switch should have a low return loss in ON state. Therefore, not only the bridge length (L_b) and width (W_b), but also lateral (L_g) and longitudinal (W_g) gaps between a bridge anchor and CPW ground have to be adjusted. This means, during optimization, those dimensions are to be simultaneously swept and determined to the optimums.

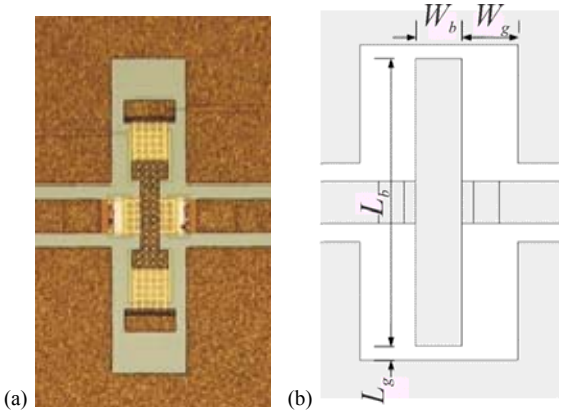

Fig. 1. Fabricated ohmic series RF MEMS switch [9] (a) and the simplified configuration (b)

III. Exploited ANN Model

The ANN model used to perform the analysis consists of four multilayer perceptron networks modeling magnitudes ($|S_{ij}|$) and for the phases ($\angle S_{ij}$) of S_{11} and S_{21} scattering (S-) parameters against the switch lateral dimensions (L_b, W_b, L_g, W_g) and frequency *f*, as shown in Fig. 2. As the switch is a symmetrical and reciprocal component, it follows that $S_{22} = S_{11}$ and $S_{12} = S_{21}$, therefore the presented model can be used to predict all four S-parameters. Each of the four ANNs has five input neurons corresponding to four mentioned lateral dimensions of the switch and the frequency. All the ANNs have only one neuron in the output layer corresponding to one of the modeled parameters ($|S_{11}|(\text{dB})$, $\angle S_{11}(\text{deg})$, $|S_{21}|(\text{dB})$ and $\angle S_{21}(\text{deg})$).

The ANN model of the considered device was developed and validated with the S-parameters data obtained from full-wave simulations with CST Microwave Studio (CST MWS) [10]. Instead of the original device layout, a simplified layout as shown in Fig. 1(b) was used. The details about training and validation of the model can be found in [8]. Trained ANN models are capable to predict the S-parameters for the given bridge geometrical parameters and frequency, enabling fast and efficient further analyses related to the bridge size adjustment in order to fulfill the design requirements.

For the analysis of reported in this paper, the ANNs modeling magnitudes of S_{11} and S_{21} have been used, as magnitude of S_{11} represents return loss and the magnitude of S_{21} represents the insertion loss. As reported in [8], the both ANNs have two-hidden-layers: the ANN modeling $|S_{11}|(\text{dB})$ has 17 hidden neurons in each of the two hidden layers, whereas the ANN modeling $|S_{21}|(\text{dB})$ has 18 hidden neurons in the first hidden layer and 16 neurons in the second hidden layer.

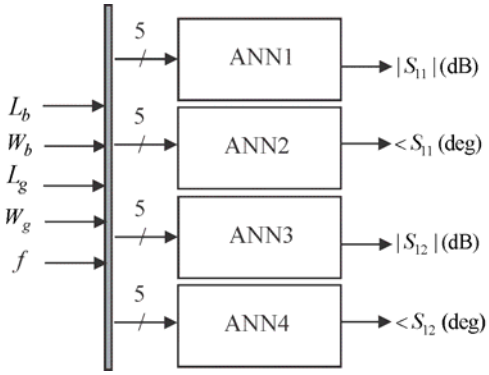

Fig. 2. ANN model of ohmic series RF MEMS switch

IV. Results and Discussion

The mentioned two ANNs have been used for further analysis of the behavior of the switch return loss and switch insertions loss with changes of the switch lateral dimensions. The analysis has been performed for the following range of the lateral dimensions: L_g - from 30 to 110 µm, L_b - from 200 to 1000 µm, W_g - from 70 to 150 µm, W_b - from 20 to 220 µm. The considered frequency range has been from 0 to 40 GHz. It should be mentioned that the above given ranges correspond to the validity range of the model, i.e. to the range of input parameters used for the model development.

For the purpose of analysis, eight differently sized devices, i.e., eight combinations of the bridge lateral dimensions have been considered.

As mentioned in Introduction, the aim of work is to analyze changes of the switch return loss caused by small changes of the dimensions in fabrication of the bridge. The considered deviations have been in the range +/- 3 µm (taken with the step of 1 µm), as that can be considered as the range of bridge fabrication tolerances in the considered technology. Moreover, besides return loss, analyses of the insertion loss changes are given. Therefore, the analysis has been performed for the deviation of the bridge dimensions L_b and W_b. First, the return and insertion loss changes when one of the two considered bridge lateral dimensions has been changed, while the others have been kept constant have been calculated by the neural model and the corresponding deviations from the expected nominal values were calculated.

The calculated deviations, i.e. maximum deviation values (absolute values) in the considered frequency range are given

TABLE I

RETURN AND INSERTION LOSS MAXIMUM DEVIATIONS - L_b CHANGES

Lb [μm]	*Wb* [μm]	*Lg* [μm]	*Wg* [μm]	Max|ΔS_{11}| [dB]	Max|ΔS_{21}| [dB]
200	20	30	70	0.5	0.0026
400	20	50	70	0.29	0.0025
300	70	90	70	0.42	0.0038
800	70	70	90	0.27	0.0054
800	20	50	110	0.54	0.0075
400	20	30	150	0.73	0.0045
1000	220	30	20	0.08	0.012
600	120	70	110	0.58	0.0063

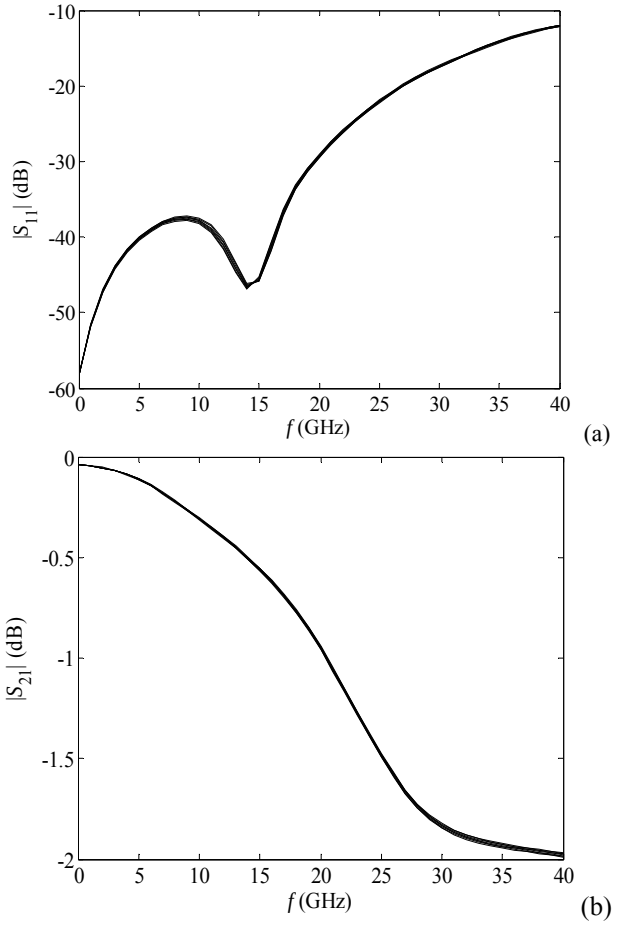

Fig. 3. Maximum influence of L_b deviation: (a) Return loss: device (400, 20, 30, 150), (b) Insertion loss: device (1000, 220, 30, 20).

TABLE II

RETURN AND INSERTION LOSS MAXIMUM DEVIATIONS - W_b CHANGES

Lb [μm]	*Wb* [μm]	*Lg* [μm]	*Wg* [μm]	Max|ΔS_{11}| [dB]	Max|ΔS_{21}| [dB]
200	20	30	70	1	0.0016
400	20	50	70	0.95	0.0092
300	70	90	70	0.83	0.0064
800	70	70	90	1.1	0.011
800	20	50	110	2.4	0.024
400	20	30	150	2.4	0.015
1000	220	30	20	0.24	0.017
600	120	70	110	1.3	0.0079

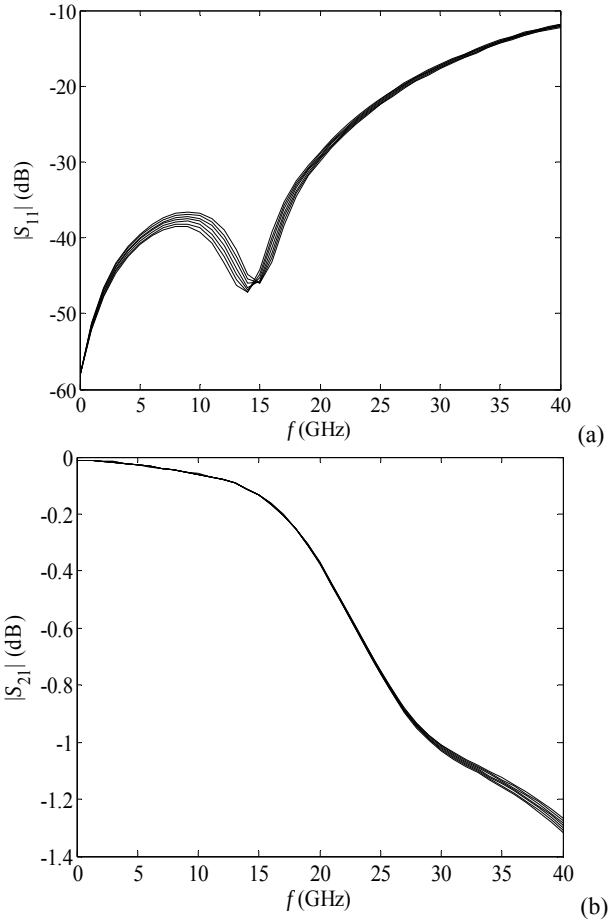

Fig. 4. Maximum influence of W_b deviation: (a) Return loss: device (400, 20, 30, 150), (b) Insertion loss: device (800, 20, 50, 110).

in Tables I and II for changes of L_b and W_b, respectively. The results show that the maximum deviation of the return loss is less than 0.73 dB for the L_b deviation and less than 2.4 dB for the W_b deviation. For the insertion loss, the deviations are less than 0.024 dB, which is significantly smaller comparing to the values of insertion loss. For illustration, in Fig. 3 and 4, the plots corresponding to devices which exhibited the maximum deviations are given. Devices are denoted as (L_b, W_b, L_g, W_g), where dimensions are given in μm.

In order to examine what happens when both dimensions are changed simultaneously in the range +/- 3 μm, keeping the gap dimensions constant, the same eight sized bridges have been considered. The maximum deviations of the return and insertion losses are depicted in Table III. The maximum deviation of the return loss is less than 3.1 dB and 0.032 dB for the insertion loss. The frequency dependence of the return and insertion loss for the devices exhibiting max deviations is shown in Fig. 5.

In all analysed cases, the insertion loss is most sensitive in frequency range from 25 to 40 GHz, where in the case of return loss the most sensitive frequency range varies with the bridge size. As expected, deviations are higher in the case of smaller sized devices.

TABLE III
RETURN AND INSERTION LOSS MAXIMUM DEVIATIONS FOR SIMULTANEOUS CHANGES OF THE L_b AND W_b UP TO +/- 3 μm

Lb [μm]	*Wb* [μm]	*Lg* [μm]	*Wg* [μm]	Max|ΔS_{11}| [dB]	Max|ΔS_{21}| [dB]
200	20	30	70	1.5	0.0036
400	20	50	70	1.2	0.012
300	70	90	70	1.3	0.01
800	70	70	90	1.4	0.016
800	20	50	110	3	0.032
400	20	30	150	3.1	0.02
1000	220	30	20	0.31	0.029
600	120	70	110	1.9	0.014

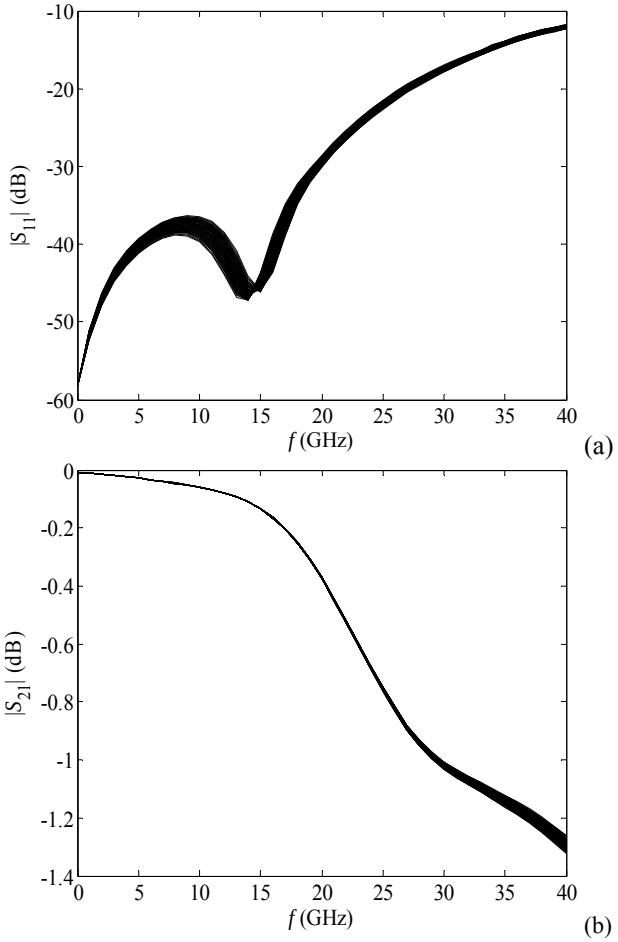

Fig. 5. Maximum influence for simultaneously deviation of L_b and W_b: (a) Return loss - device (400, 20, 30, 150), (b) Insertion loss - device (800, 20, 50, 110).

V. CONCLUSION

In this paper an ANN model of ohmic series RF MEMS switch has been applied to obtain and analyze the switch return and insertion losses versus the switch bridge lateral dimensions. Since the model has very short response time, the analysis was performed in significantly shorter time that it would be needed in standard electromagnetic simulators. The influence of small changes of the bridge lateral dimensions caused by the fabrication process on the return and insertion losses has been studied. It is shown that the deviation of the switch lateral dimensions during fabrication process cause deviations of the return and insertion loss. However, in all considered case, the deviations of the insertion loss are almost negligible, while in the case of return loss the deviations can be up to around 3 dB. Therefore, taking care about the frequency range of interest, it is recommended to set the optimization goal for the return loss to be a few dB smaller that the requested value in order to ensure that, even with the deviation of the bridge dimensions during the fabrication, the return loss is below the desired value.

ACKNOWLEDGEMENT

This work was funded by the bilateral Serbian-German project "Smart Modeling and Optimization of 3D Structured RF Components" supported by the DAAD foundation and Serbian Ministry of Education, Science and Technological Development. The work was also supported by the projects III-43012 and TR-32052 of the Serbian Ministry of Education, Science and Technological Development.

REFERENCES

[1] G. M. Rebeiz, *RF MEMS Theory, Design, and Technology*, New York, Wiley, 2003.

[2] L. Vietzorreck, "EM Modeling of RF MEMS," 7th International Conference on Thermal, *Mechanical and Multiphysics Simulation and Experiments in Micro-Electronics and Micro-Systems*, EuroSime, pp.1-4, Como, Italy.

[3] M. A. Llamas, D. Girbau, E. Pausas, L. Pradell, S. Aouba, C. Villeneuve, V. Puyal, P. Pons, R. Plana, S. Colpo, F. Giacomozzi, "Capacitive and Resistive RF-MEMS switches 2.5D & 3D Electromagnetic and Circuit Modeling", Spanish Conference on Electron Devices, 2009. CDE 2009, pp.451-454, 11-13 Feb. 2009.

[4] Q. J. Zhang and K. C. Gupta, *Neural Networks for RF and Microwave Design*, Boston, MA, Artech House, 2000.

[5] H. Kabir, L. Zhang, M. Yu, P. Aaen, J. Wood, and Q. J. Zhang "Smart Modelling of Microwave Devices", *IEEE Microwave Magazine*, vol. 11, no. 3, pp.105–108, 2010.

[6] Y. Lee, D. S. Filipovic, "Combined Full-wave/ANN based Modelling of MEMS Switches for RF and Microwave Applications," *Proc. of IEEE Antennas and Propagation Society International Symposium*, vol. 1A, pp. 85-88, Washington DC, USA, 2005.

[7] Y. Gong, F. Zhao, H. Xin, J. Lin, Q. Bai, "Simulation and Optimal Design for RF MEMS Cantilevered Beam Switch," *Proc. of International Conference on Future Computer and Communication* (FCC '09), pp. 84-87, Wuhan, China, 2009.

[8] M. Milijić, Z. Marinković, T. Kim, O. Pronić-Rančić, L. Vietzorreck, V. Marković, "Modeling and optimization of ohmic series RF MEMS switches by using neural networks," *8th German Microwave Conference, GeMiC 2014*, Aachen, Germany, March, 2014, pp. 1-4.

[9] S. DiNardo, P. Farinelli, F. Giacomozzi, G. Mannocchi, R. Marcelli , B. Margesin, P. Mezzanotte, V. Mulloni, P. Russer, R. Sorrentino, F. Vitulli, L. Vietzorreck, "Broadband RF-MEMS based SPDT", *Proc. European Microwave Conference 2006*, Manchester, Great Britain, September 2006.

[10] CST MICROWAVE STUDIO® 2012.